HIGH RESOLUTION NANOIMPRINT FOR NANOPHOTONICS

A Dissertation

by

YOUWEI JIANG

Submitted to the Office of Graduate and Professional Studies of
Texas A&M University
in partial fulfillment of the requirements for the degree of

DOCTOR OF PHILOSOPHY

Chair of Committee,	Xing Cheng
Committee Members,	Lin Shao
	Kamran Entesari
	Jun Zou
Head of Department,	Chanan Singh

May 2014

Major Subject: Electrical Engineering

Copyright 2014 Youwei Jiang

ABSTRACT

Nanophotonics have drawn huge attention in recent years in various applications. Surface sensing technique, including surface-enhanced Raman spectroscopy (SERS), is an important topic of nanophotonics and has been widely investigated. The capability of SERS-active device depends on two main factors: good reproducibility and high enhancement factor. Ordered metallic nanostructures with high resolution are usually preferred for SERS application. Nanoimprint lithography can provide a low-cost and high resolution fabrication technique for SERS-active devices.

The objective of this research is to explore the application of nanoimprint lithography in SERS-active devices. This work begins with two issues of nanoimprint lithography: mold fabrication and throughput improvement. The potential of nanoimprint lithography depends on reliable mold fabrication. Two techniques are investigated, which are polyelectrolyte electrostatic self-assembly and controlled polymer reflow. Based on the observation of exceptional thermal stability of entangled polymer, step-and-repeat thermal nanoimprint lithography is developed. This technique significantly improves the throughput and enables the large scale application of thermal nanoimprint.

Ordered metallic nanostructures have been widely used as SERS-active substrates. In order to achieve high enhancement, extremely high resolution is needed, which can be limited by lithography technique. In this work, SERS-active devices based on gap

surface plasmon polaritons are fabricated by nanoimprint lithography. 17 times more enhancement is achieved compared with conventional SERS-active devices on the same structure dimensions. This technique opens up possibilities of single molecule detection in the future.

ACKNOWLEDGEMENTS

I would like to express my deep respect and gratefulness to my PhD advisor, Dr. Xing Cheng. He has provided me great support and wide knowledge through my doctoral studies. I also would like to thank my committee members, Dr. Lin Shao, Dr. Kamran Entesari and Dr. Jun Zou for their guidance and support throughout the course of this research.

Thanks also go to my group colleagues, Dehu Cui, Huifeng Li, Taohua Lee, Yi-chen Lo, Wonsuk Lee, Gihoon Choo, Bingqing Luo, Ning Xia, Binhao Wang and Yunbum Jun. I would like to thank them for friendship and help.

Thanks to my mother and father for their support and encouragement.

Thanks for my wife for her sacrifice and love.

TABLE OF CONTENTS

Page

ABSTRACT ii

ACKNOWLEDGEMENTS iv

TABLE OF CONTENTS v

LIST OF FIGURES vi

LIST OF TABLES ix

CHAPTER I INTRODUCTION TO NANOIMPRINT LITHOGRAPHY 1

1.1. Nanoimprint mold 3
1.2. Nanoimprint resist 4
1.3. Current issues and the organization of the dissertation 5

CHAPTER II HIGH RESOLUTION NANOIMPRINT MOLD FABRICATION 6

2.1 Nanoimprint mold fabrication by electrostatic self-assembly 6
2.2 Nanoimprint mold feature size reduction by metal sputter deposition 16
2.3 Nanoimprint mold with reduced feature size by controlled PMMA reflow 18
2.4 Controlled reflow based on exceptional thermal stability of polycarbonate 24

CHAPTER III STEP-AND-REPEAT THERMAL NANOIMPRINT 38

3.1 Introduction to step-and-repeat nanoimprint 39
3.2 Step-and-repeat thermal nanoimprint 41
3.3 Polymer chain entanglement 47

CHAPTER IV THE APPLICATION OF NANOIMPRINT IN NANOPHOTONICS 53

4.1 Sensitive SERS substrate based on gap surface plasmon polaritons 55

CHAPTER V SUMMARY 70

REFERENCES 72

LIST OF FIGURES

Page

Figure 1. Schematics of thermal nanoimprint and UV nanoimprint. 2

Figure 2. The schematic of electrostatic self-assembly technique. 8

Figure 3. Molecular structure of (a) PDDA and (b) PSS. 8

Figure 4. The plot of bilayer thickness as a function of bilayer numbers. 10

Figure 5. (a) Original Si mold with 50 nm diameter hole array; (b) Si hole array with 10 PDDA: PSS bilayer growth; and (c) Si hole array with 20 PDDA:PSS bilayer growth. Inserts are at higher magnitude. 11

Figure 6. Schematics of electrostatic self-assembly film deposition on gold structures. 15

Figure 7. Gold gratings after self-assembled film removal. 16

Figure 8. (a) Top view of modified nanoimprint mold after 8 nm metal deposition by sputtering; (b) Cross-sectional view of the modified nanoimprint mold. 17

Figure 9. Schematic of PMMA pattern controlled reflow. 19

Figure 10. Fabrication procedure of nanoimprint mold with reduced feature size by PMMA controlled reflow. Left: Schematics of polymer pattern modification by controlled polymer wetting: (a) sample prepared by Cr evaporation and PMMA spin-coating; (b) PMMA patterning by nanoimprinting and oxygen RIE; (c) PMMA re-patterning by thermal annealing; (d) Cr wet etching with PMMA mask, which is then removed by acetone; (e) SiO_2 dry etching by CHF_3 RIE with Cr mask, followed by Cr removal. Right: (a) sample prepared by Cr evaporation and PMMA spin-coating; (b) PMMA patterning by nanoimprinting and oxygen RIE; (c) PMMA re-patterning by thermal annealing; (d) SiO_2 dry etching by CHF_3 RIE with PMMA mask; (e) PMMA mask removal by acetone. 21

Figure 11. (a) Original PMMA square array pattern formed by nanoimprint; residue layer was removed; the spacing between two square is c.a. 350 nm; (b) modified PMMA patterns by thermal annealing at 150oC for 150 seconds; (c) chromium patterns obtained from (b) by chemical wet etch; the spacing between two dots is c.a. 80 nm. 22

Figure 12. (a) Original 350 nm gratings nanoimprinting mold with duty cycle of 50%; and (b) modified SiO2 gratings with duty cycle of 77%. 24

Figure 13. A schematic of (a) polycarbonate resist patterned by NIL on chromium layer and grating height controlled by oxygen RIE; (b) sample annealed on hotplate at elevated temperature and (c) stable structures formed by polymer reflows regardless of annealing time. 29

Figure 14. (a) polycarbonate pillars without thermal annealing and (b) polycarbonate pillars with 300 ^{o}C thermal annealing for 30 min. 31

Figure 15. Statistical distribution of polycarbonate pillar radius: no annealing on the top and 30 min 300 ^{o}C annealing on the bottom. 31

Figure 16. (a) polycarbonate gratings (700nm pitch, 50% duty cycle and ca.150 nm height) fabricated by thermal NIL and oxygen RIE; (b) polycarbonate gratings after thermal annealing at 200 ^{o}C for 30 min; (c) SiO_2 gratings by CHF_3 RIE from (b); and (d) SiO_2 gratings by CHF_3 RIE from polycarbonate gratings with ca.70 nm height. Inserts are at higher magnification. 33

Figure 17. The plot of trench sizes after thermal annealing on chromium (square) and SiO_2 (triangle) substrate as a function of the initial height of the grating before thermal annealing. 34

Figure 18. Polycarbonate gratings with trench size of 35.0±5.2 nm after thermal annealing. 36

Figure 19. The plot of trench sizes with respect to the annealing time. The initial height for the grating patterns before annealing is 70 nm. 36

Figure 20. Photography of a substrate imprinted by two sequential steps of step-and-repeat process. 42

Figure 21. Trench size of grating structures fabricated by two sequential nanoimprint steps by step-and-repeat process: 90 nm resist imprinted at 150 ^{o}C with (a) step 1 and (b) step 2; 40 nm resist imprinted at 150 ^{o}C with (c) step 1 and (d) step 2; 20 nm resist imprinted at 150 ^{o}C with (e) step 1 and (f) step 2; 20 nm resist imprinted at 200 ^{o}C with (g) step 1 and (h) step 2. 44

Figure 22. AFM profile of step-and-repeat thermal nanoimprint of 20 nm polycarbonate resist: profile of step 1 (a) and section information (b); profile of step 2 (c) and section information (d). 46

Figure 23. Grid structures fabricated by dual nanoimprint of step-and-repeat process at orthogonal directions on 90 nm polycarbonate resist; inserts are at higher magnitude. 47

Figure 24. X-ray diffraction spectrum of 20 nm polycarbonate resist spin-coated on Si wafer (black) and after step-and-repeat thermal NIL (purple). 49

Figure 25. Schematics of three different SERS-active substrates: (a) type 1, a conventional SERS-active substrate with silver grids on the bottom silver layer; (b) type 2, a uniform SiO_2 spacer sandwiched between the top silver grids and the bottom silver layer; and (c) type3, both top silver grids and the SiO_2 spacer are patterned on the bottom silver layer. The interfaces are labelled as 1, 2 and 3 for easy reference in the discussion section. 59

Figure 26. The schematic of metal/insulator/metal structure. 60

Figure 27. Schematics of the fabrication flow for type 1,2 and 3 SERS-active substrates: (a) 200 nm bottom silver layer evaporation on Si wafer; (b2) 20 nm SiO_2 spacer evaporation on bottom silver layer and (b) PMMA pattern definition by nanoimprint lithography; (c) oxygen reactive ion etching to remove the residual layer; (d1),(d2) 40 nm top silver layer evaporation and (d3) sequential evaporation of 20nm SiO_2 spacer and 40 nm top silver layer; (e) lift-off process in acetone with ultrasound agitation. 61

Figure 28. The SEM top view of fabricated type 2 SERS-active substrate by nanoimprint. The scale bar is 1 um. 64

Figure 29. Raman spectra of thiophenol from type 1, type 2, type 3 SERS-active substrates and the reference sample (scaled down by 10^{-2}). The intensity of 1072 cm^{-1} peak is labeled. All spectra were collected under the same conditions. 65

Figure 30. Plots of field intensity distribution along the interfaces of different substrates (See Fig.25 for interface labeling). The dimension of all top patterns is 600 nm and the wavelength of the incident light is 633 nm. All plots are taken from the edge of the interface. The values of the peak intensities are 33.0 (type 1-1), 27.1 (type 3-1), 13.3 (type 2-1), 2.7 (type 3-3) in (a) and 246.7 (type 2-2), 142.5 (type 3-2), 3.6 (type 1-2) in (b). 65

Figure 31. FDTD calculation of intensity distribution of type 2 substrate with (a) 20 nm SiO_2 spacer; (b) 50 nm SiO_2 spacer and (c) 80 nm SiO_2 spacer. The arrow represents the propagating direction of the incident light. 69

LIST OF TABLES

Page

Table 1. Modified pattern spacing at 150 ^{o}C. 23

CHAPTER I

INTRODUCTION TO NANOIMPRINT LITHOGRAPHY

Nanoimprint lithography (NIL) has drawn huge attention as one of the most important next generation lithography techniques. NIL was initially invented by Chou[1] and is featured by low-cost, high resolution and easy fabrication. In principal, nanoimprint lithography is a non-conventional lithography technique based on the mechanical deformation of imprint resist. Basically NIL can be categorized into thermal NIL and UV NIL. Figure 1 illustrates the schematics of thermal NIL and UV NIL. For thermal NIL, thermal plastic resist was prepared on the substrate by spin-coat and heated up to be above the material's glass transition temperature (T_g). At temperatures above T_g, the resist material is deformable due to higher viscosity and NIL mold is applied onto the resist layer with elevated pressure. Patterns are defined in contrast to the NIL mold patterns. After cooling down to temperatures below T_g, NIL mold is released from the resist and polymer structures are formed. In order to separate the mold from the resist, the NIL mold is usually coated with low surface energy surfactant. After imprint, there usually exists a thin layer of resist underneath the patterns, which is referred as "residue layer", and oxygen reactive ion etch can be applied to remove this thin layer for succeeding applications. For UV nanoimprint, UV curable imprint resist is applied on the substrate and pressed by a transparent imprint mold with relative low pressure. Then UV radiation is applied and the resist will be cured and hardened, followed by mold release. In this chapter, we will present the basic concepts of nanoimprint lithography.

Then we will discuss applications in NIL techniques and the issues addressed in this work.

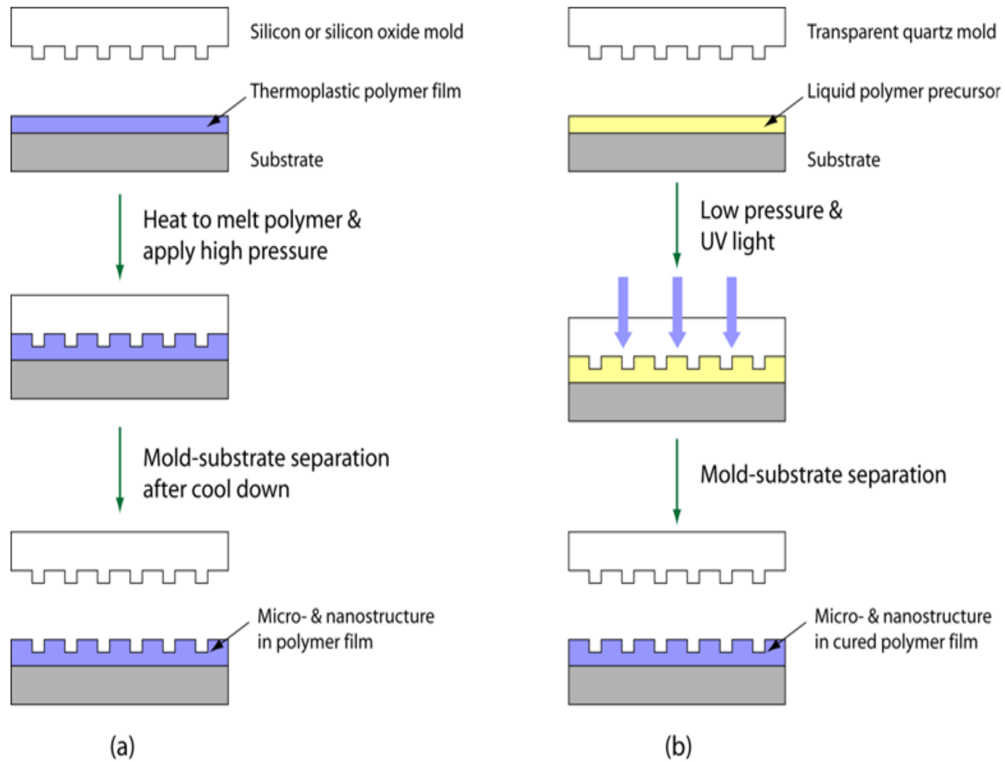

Figure 1. Schematics of thermal nanoimprint and UV nanoimprint.

1.1 Nanoimprint mold

The potential of the high resolution of NIL relies on NIL mold with high quality nanostructures. NIL mold is usually fabricated by optical lithography or electron beam lithography, followed by dry etch into hard materials. Si and SiO_2 are commonly used as NIL mold not only because of hardness and high durability but also of the compatibility with micro fabrication process. In addition, since thermal NIL is usually conducted at elevated temperatures, the thermal expansion of NIL mold can impact the quality of patterning. Therefore Si based NIL mold is preferred as it is able to match the expansion coefficient of the Si substrate and can be processed by dry etch. Transparent quartz mold is widely used for UV NIL. Except for Si and SiO_2 mold, materials such as Ni[2], SiC[3] and diamond[4] has been investigated as NIL mold materials.

As the NIL mold contains high density of nanostrucutres, the large surface area interacted by NIL mold and resist results in extremely large adhesion, which leads to difficult separation between the mold and resist. A common defect of NIL can be the peeling of resist off the substrate by mold release. In order to circumvent this issue, an anti-adhesive monolayer is usually applied to the mold surface. 1H, 1H, 2H, 2H-perfluorodecyltriethoxysilane (FDTS) is a commonly used surfactant which significantly reduced the surface energy of the mold surface, by attaching the Si-based surface with silane group and generating low-energy fluorinnated group. FDTS can be applied by vapor evaporation or in solvent phase. In the vapor phase method, FDTS vapor is evaporated onto the mold surface at elevated temperature. In the solvent phase method,

NIL mold is immersed into FDTS solvent in heptanes for 10 min and thoroughly rinsed in heptanes. After that the mold is completely dried by N_2 gas and thermal annealing. In our work, the solvent phase method is preferred due to better uniformity and the capability of self-assembled monolayer. The anti-adhesive layer can be removed by oxygen reactive ion etch and deposited again in case of possible decreasing durability.

1.2 Nanoimprint resist

Nanoimprint lithography is a mechanical deformation process which relies on the deformable capability of the resist materials. Thermal plastic polymers are commonly used resist materials. For a typical thermal plastic polymer, it remains glassy and difficult to pattern at low temperature. As the temperature increase to glass transition temperature, local motion of polymer chains start to take place and the modulus of the polymer dramatically deceases. At higher temperatures, the viscosity of the polymer becomes really high and the resist behaves like liquid. The temperature of thermal NIL is usually chosen to be above T_g but below liquid phase region.

Materials with relatively lower T_g is preferred for high-throughput fabrication. As we know that the resist needs to be heated above T_g for deformation and cooled to be below T_g for mold separation, low T_g materials can be better for throughput and reducing the thermal expansion. However, another important criterion for NIL resist is to maintain good integrity after the pattern formation. Therefore low T_g materials can suffer from

pattern decay in room temperature. As a result, proper materials need to be selected in consideration of easy deformation and good mechanical integrity.

1.3 Current issues and the organization of the dissertation

Although NIL is a promising next generation lithography technique featured with high resolution, low cost and easy fabrication, there remains some issues. Traditional method for NIL mold fabrication is electron beam lithography, which is characterized by extremely high resolution. However low throughput and high cost of this technique is of concern. In chapter Ⅱ we will present novel techniques for high resolution NIL mold fabrication with low cost. Sub-50 nm resolution NIL mold is fabricated based on polymer pattern reflow and 1 nm resolution fabrication technique is reported based on polymer electrostatic self-assembly.

Compared with UV NIL, thermal NIL is preferred in fields such as functional polymer patterning because of the possible degradation of the material upon UV radiation. However thermal NIL suffers from low throughput due to the thermal cycle of heating and cooling for a single imprint. Moreover, multi imprints within the same substrate is not available for thermal NIL as the heating during NIL can damage the previous patterns. Based on our observation towards entangled polymer resist, we developed a unique thermal NIL implemented in a step-and-repeat fashion in chapter Ⅲ. In chapter Ⅳ we explored the application of NIL in surface sensing techniques and fabricated a sensitive SERS substrate with high enhancement factor and easy fabrication.

CHAPTER II

HIGH RESOLUTION NANOIMPRINT MOLD FABRICATION

As we have discussed in the introduction part, nanoimprint lithography is characterized as super-high resolution in pattern replication. However the potential of nanoimprint fabrication depends on the ability of nanoimprint mold fabrication. For conventional top-down fabrication technique such as electron-beam lithography (EBL), it is reliable to pattern nanostructures in 20 nm scale while the reliability can suffer great degradation with patterns of higher density. In addition, other significant disadvantages of EBL are low throughput and huge cost[5]. In order to continuously reduce the feature size of nanoimprint mold, preferably down to sub-10 nm, we presented and carried out two techniques in our research work, which are pattern size reduction by electrostatic self-assembly and pattern size modification by controlled polymer reflow.

2.1 Nanoimprint mold fabrication by electrostatic self-assembly

Electrostatic self-assembly (ESA) is a layer-by-layer thin film deposition technique relying on the electrostatic interactions between polyelectrolyte[6]. Since the resolution of this technique depends on the thickness of the ESA bilayer, which is on the order of 0.5 to greater than 5 nm[7], it can well meet the requirement for sub-10 nm nanofabrication. In addition, compared with conventional electron beam lithography, which is high cost with limited throughput, ESA is a low cost technique with wafer-size process capability. The schematic of ESA process is illustrated in Figure 2. First the substrate is pre-treated so

that the surface is positively or negatively charged. Then a layer of polyanion is applied to the positively charged substrate by immersing the substrate into the polyanion solution. A uniform polyanion layer can be adsorbed due to the electrostatic attraction between the opposite charges while the excessive polyanion can be repelled as long as the charged surface is completely occupied. After removing the loose polymer chains by thorough wash in DI water, the substrate is transferred to polycation solution for another layer deposition, followed by another DI water rinse. If the substrate is pre-treated to be negatively charged, the application of polyanion and polycation is reversed. The process of bilayer deposition can be repeated for multiple bilayer growth and final film thickness is determined by the number of bilayer and the thickness of a single bilayer at the same time, as well as the deposition parameters.

Varieties of substrate and materials can be selected for ESA technique depending on practical applications. Our goal is for sub-10 nm fabrication for nanoimprint and therefore we present in this work the technique using polydiallyldimethylammonium chloride (PDDA), acting as polycation, and sodium polystyrene sulfonate (PSS), serving as polyanion (Figure 3), onto 50 nm Si patterns as the starting substrate.

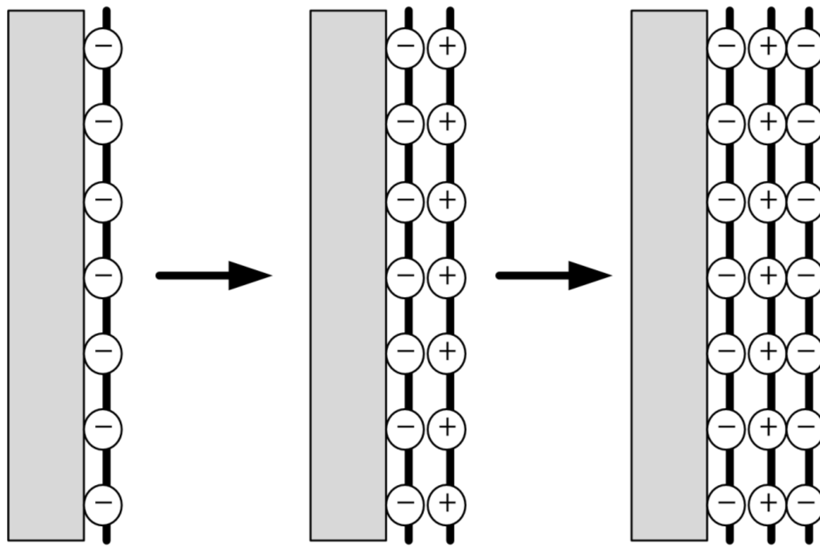

Figure 2. The schematic of electrostatic self-assembly technique**.**

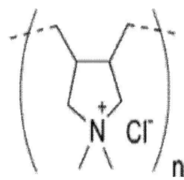

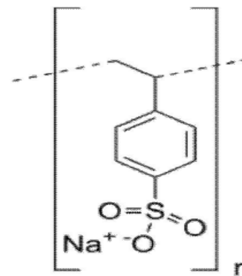

(a) (b)

Figure 3. Molecular structure of (a) PDDA and (b) PSS.

2.1.1 Substrate and materials

Different substrates such metals[8], Si/SiO_2, polymer and carbon nanotube[9] have been reported for ESA applications. Considering the compatibility of Si/SiO_2 with nanoimprint mold, we use Si substrate with 50 nm holes defined by electron beam lithography. PDDA and PSS are selected as polycation and polyanion, respectively. 0.2 wt% water solution for PDDA and PSS are prepared as the content for ESA film.

2.1.2 Substrate pre-treatment

Piranha solution is used to pre-treat the surface of Si nano-structures. Piranha solution was prepared by mixing 35% H_2O_2 and concentrated H_2SO_4 with the ratio of 30% to 70%. Then Si mold with 50 nm hole array was cleaned in the piranha solution for 20 minute, followed by 15 minute substrate rinse in water. The Si substrate was negatively charged after the piranha treatment due to the hydroxyl group on the surface. Oxygen reactive ion etching can also be used to treat the Si surface.

2.1.3 Bilayer deposition

After pre-treatment, the Si substrate was dipped into 0.2 wt% PDDA water solution for 1 minute with ultrasound treatment. We applied ultrasound vibration here to assist the polymer chains to move into the holes of the Si mold in order to achieve uniform polymer coverage all over the patterns. Then the Si substrate was fully rinsed in DI water and dried by N_2 blow and baking at 75 ^{o}C for 1 minute. After that, the Si substrate was dipped into 0.2 wt% PSS water solution for 1 minute with ultrasound treatment,

followed by the same rinse and drying procedure. The final thickness of bilayer deposition was controlled by the number of deposition process.

2.1.4 Results and discussion

In order to characterize the precision of this technique, we acquired the single bilayer thickness by applying the deposition on plain Si wafer. ESA film thickness was measured by Nanofilm EP3-SE imaging ellipsometer. Figure 4 shows the increasing film thickness with more layers deposited. Around 0.5 nm resolution for one bilayer can be estimated from the plots.

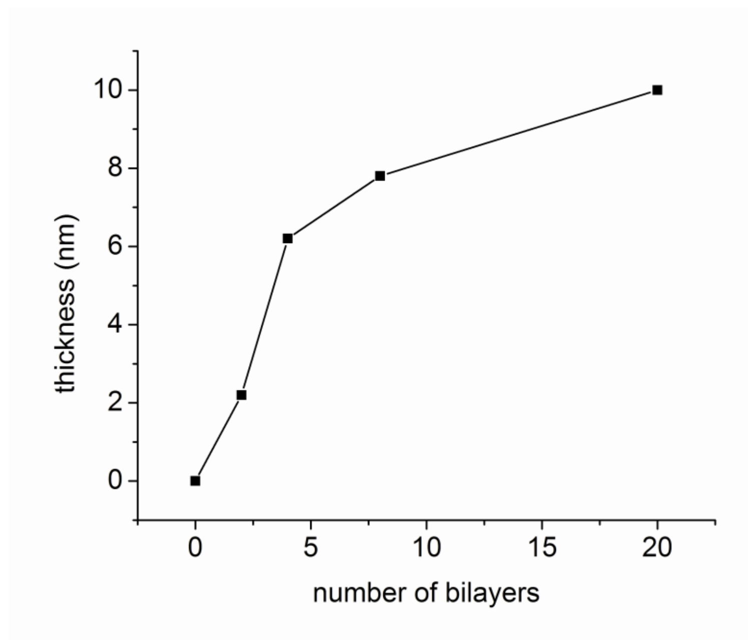

Figure 4. The plot of bilayer thickness as a function of bilayer numbers.

For Si substrate with 50 nm diameter holes, we obtained modified features with reduced diameter after ESA deposition. The SEM images of original Si mold, the Si mold with 10 bilayers and 20 bilayers were shown in Figure 5. By applying 10 and 20 ESA bilayers onto 50 nm hole patterns, the diameter of the holes were reduced by 10 nm and 20 nm respectively. And uniformly modified patterns could be observed from the SEM images. On average, about 0.5 nm of one bilayer thickness was deduced from the SEM results. In other words, this PDDA:PSS bilayer growth technique has a precision on the order of half nanometer, which is perfect for nanoscale feature size modification down to sub-10 nm.

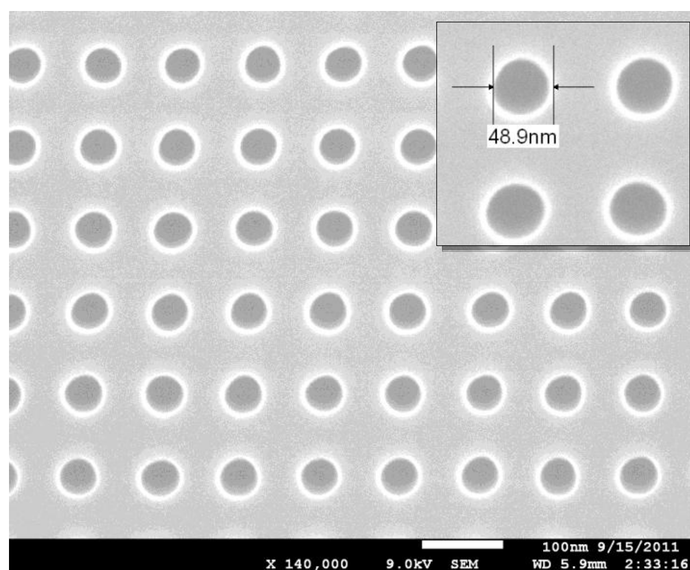

(a)

Figure 5. (a) Original Si mold with 50 nm diameter hole array; (b) Si hole array with 10 PDDA: PSS bilayer growth; and (c) Si hole array with 20 PDDA:PSS bilayer growth. Inserts are at higher magnitude.

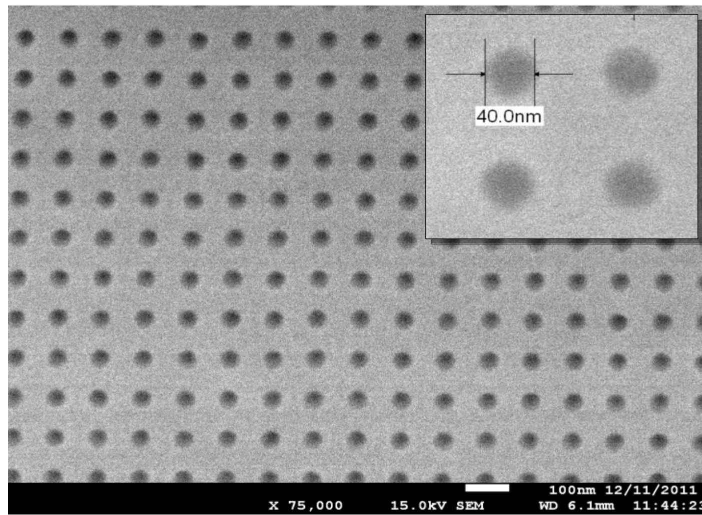

(b)

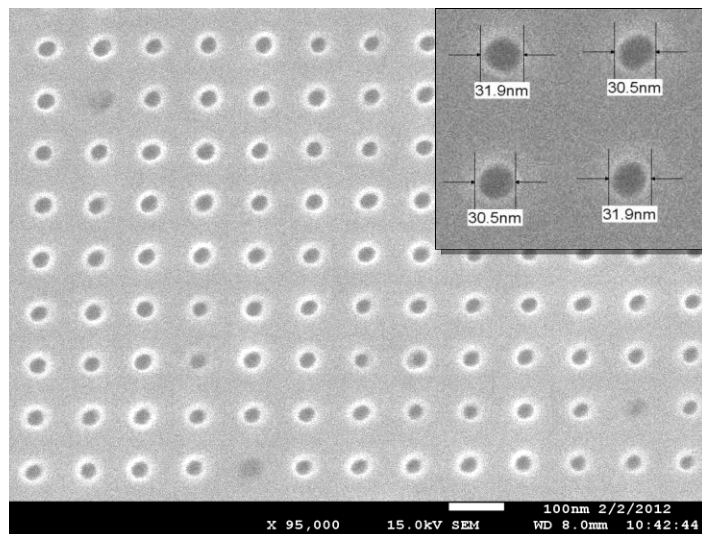

(c)

Figure 5. Continued

By ESA film deposition we acquired nano-structures with reduced feature size with 0.5 nm precision. However the modified structures cannot be directly used as a nanoimprint mold due to the instability of ESA film under high temperature and pressure during thermal nanoimprint. The modified features need to be transferred into the Si substrate for nanoimprint application. However so far we cannot achieve this since the ESA film is deposited not only along the side walls but also on the bottom of the hole patterns. In order to solve this issue, we investigated the electrostatic-self assembly technique on gold structures and this will be discussed in the following section.

In summary, ESA bilayer growth is a promising technique for super-high resolution nanoscale pattern modification due to its high uniformity and precision. In addition, the procedure of ESA bilayer growth is simple because it is a self-assembled process. The overall thickness of ESA layers can be easily controlled by bilayer numbers. However on the other hand, since we started with 50 nm feature size structures, at least 40 PDDA:PSS bilayers are required to achieve sub-10 nm feature size, which is expected to be a time consuming and tedious work.

2.1.5 Polymer electrostatic self-assembly on gold structure

As we presented in the previous section, electrostatic self-assembly film deposition on Si substrate has a precision as high as 0.5 nm with good uniformity and therefore may be a good candidate for sub-10 nm nanoimprint mold fabrication. However although we were able to achieve sub-30 nm feature size on Si substrate, unfortunately the sub-30 nm

structures cannot be directly used as the nanoimprint mold due to the low mechanical strength of the self-assembly materials. And at the same time, we could not figure out a good method to transfer the sub-30 nm structure to the substrate material. In order to overcome these issues, we investigated self assembly technique on gold structures.

Figure 6 illustrates the self-assembly deposition procedure on gold structure. The major difference between self-assembly film deposition on gold and Si results from the first layer deposition. For ESA on Si, the substrate is pre-treated to contain surface charges so that the polyelectrolyte can be deposited due to electrostatic interaction. For the self-assembly on gold surface, polymer with thiol group (-SH) is selected due to its affinity towards noble metal[10]. In this work, 16-mercaptoalkanoic acid ($SH(CH_2)_{15}COOH$) and $Cu(ClO_4)_2$ are used as polyanion and cation. The film deposition procedure is similar to ESA process on Si substrate. First gold gratings (700 nm pitch and 50% duty cycle) with 40 nm height were fabricated by nanoimprint lithography (Figure 6 (a)-(c)). Then the self-assembly film was deposited by alternative substrate incubation in 1mM 16-mercaptoalkanoic acid water solution for 1 hour and 1mM $Cu(ClO_4)_2$ for 15 min. Complete rinse in DI water and drying was done before each deposition and there were five bilayers in total . After the self-assembled film was formed on gold structure (Figure 6 (d)), 40 nm gold film was evaporated by electron beam evaporation onto the substrate (Figure 6 (e)), which was then followed by 5% HCl rinse to remove the self-assembled film. After that gold gratings were left behind with reduced feature size, which was determined by the thickness of the self-assembled film (Figure 6 (f)). Figure 7 shows the

gold gratings with reduced trench size on the order of 20 nm. However rough edges can be observed, which are definitely not desirable. The hazy trenches could be ascribed to two reasons. First the starting gold gratings were fabricated from evaporation and lift-off, which could introduce irregular grating outline. Second, even a single chain of 16-mercaptoalkanoic acid could be too long for sub-10 nm resolution, where polymers with smaller molecular weight (better resolution and uniformity) may be more desirable.

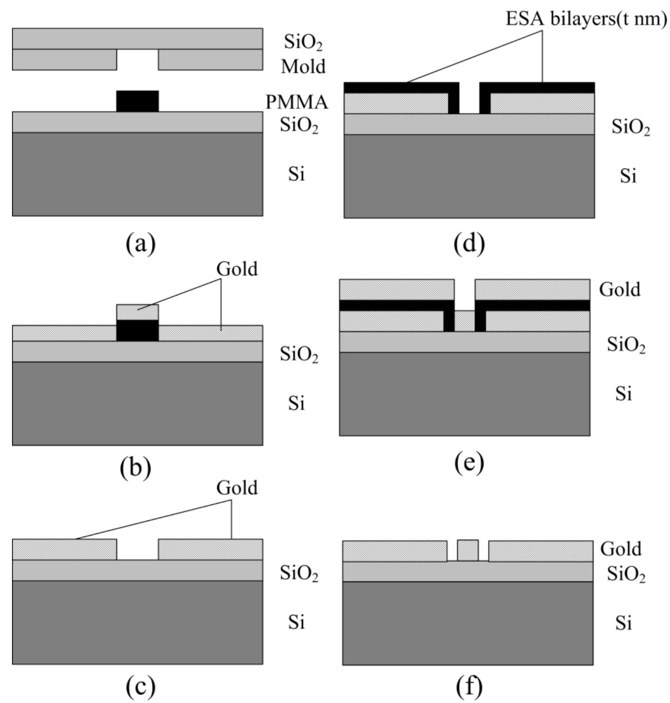

Figure 6. Schematics of electrostatic self-assembly film deposition on gold structures.

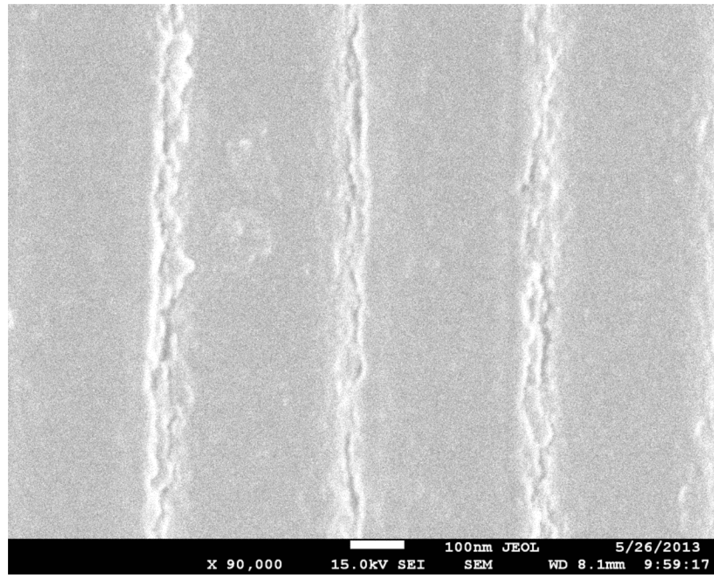

Figure 7. Gold gratings after self-assembled film removal.

2.2 Nanoimprint mold feature size reduction by metal sputter deposition

Another technique we developed to fabricate modified-feature-size nanoimprint mold is also based on material deposition with nanoscale precision. Metal deposition by sputtering was directly applied onto the surface of nanoimprint mold. Due to uniformity and rapidness of metal sputter deposition, nanoimprint mold with uniformly modified patterns could be fabricated effortlessly.

Experimentally 8 nm Pd/Pt was sputtered onto the nanoimprint mold with 50 nm hole array. The SEM images of the modified mold were presented in Figure 8. The uniformity of the overall morphology of the modified patterns must be a concern for nanoimprint mold. Vertical sidewalls are desirable instead of trapezium morphology for

nanoimprint application. Vertical sidewalls were observed by SEM in Figure 8(b) and the pattern size shrunk from 50 nm to around 30 nm. The cross-section view of the structures indicates uniform sidewall coverage. This is because during sputtering, the chamber pressure is maintained at a level that results in short mean-free path for gaseous species, and consequently conformal instead of direction deposition is achieved. Due to its simplicity, this technique is still promising due to its uniformity and convenience.

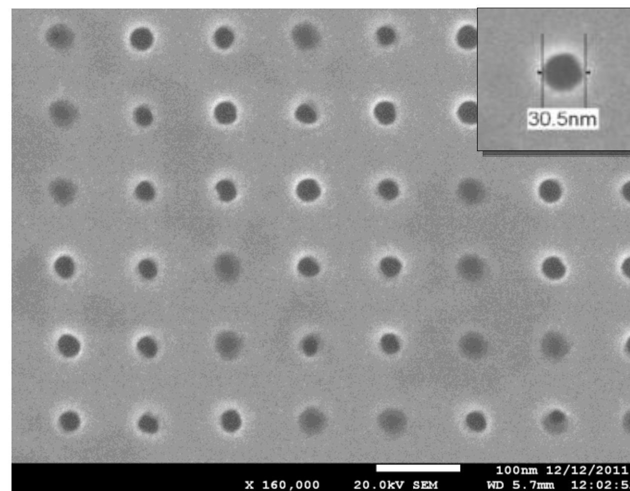

(a)

Figure 8. (a) Top view of modified nanoimprint mold after 8 nm metal deposition by sputtering; (b) Cross-sectional view of the modified nanoimprint mold.

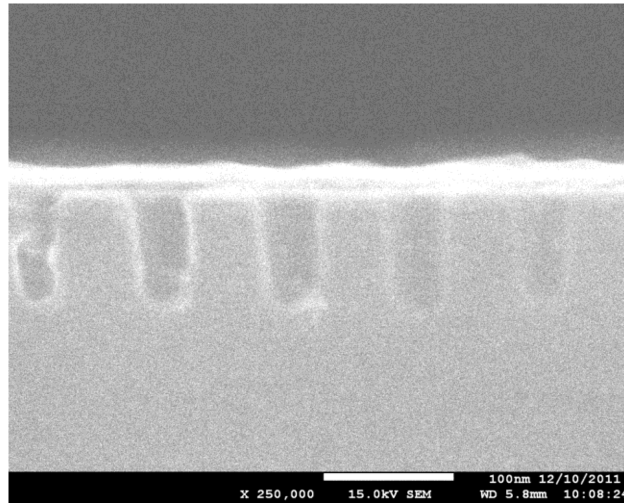

(b)

Figure 8. Continued.

2.3 Nanoimprint mold with reduced feature size by controlled PMMA reflow

Poly (methyl methacrylate) (PMMA) is a thermal plastic polymer and is widely used as a thermal nanoimprint resist. As we discussed in the introduction part, thermal nanoimprint is an embossing technique that the thermal plastic resist is heated above the glass transition temperature (T_g) and patterned by hard mold under pressure. Heated above $T_{g,}$ which is 105°C, the viscosity of PMMA is significantly reduced and can be defined with the confinement of the nanoimprint mold. However if existing PMMA patterns are annealed above T_g without any confinement, the PMMA patterns will spread on the substrate until an equilibrium state is achieved. With careful control of annealing time and temperature, the spacing between the PMMA patterns can be reduced before

merge. Figure 9 illustrates the controlled reflow process with PMMA cubes as the starting patterns.

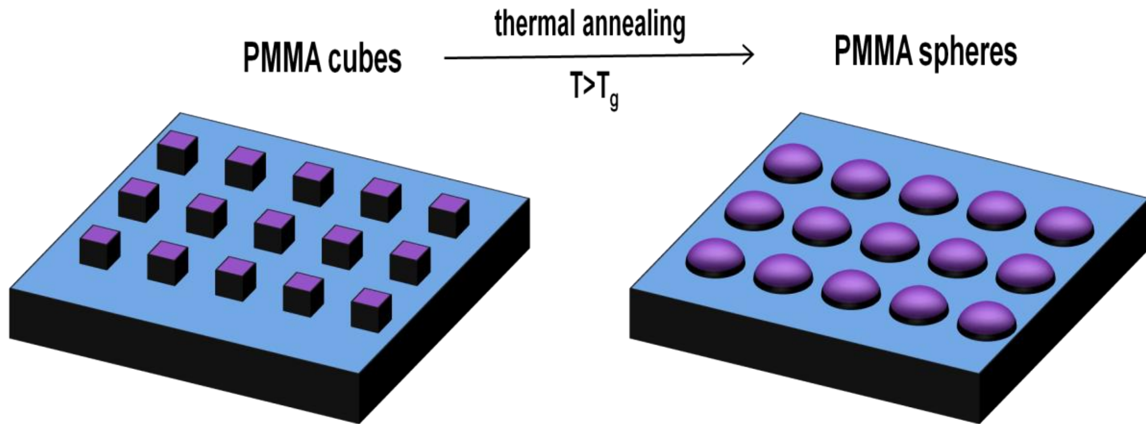

Figure 9. Schematic of PMMA pattern controlled reflow.

2.3.1 Experimental details

Figure 10 illustrates two alternative methods for the fabrication of nanoimprint mold with reduced feature size. Shown as Figure 10 (left) nanoimprint is done with PMMA, which is spin-coated on a substrate stack of chromium, SiO_2 and Si. After nanoimprinting and residual layer removal, isolated PMMA pillars are formed. Then the sample is annealed at elevated temperature above the glass transition temperature for PMMA. Due to polymer reflow, the pattern size of PMMA is therefore modified and the spacing between the isolated patterns is reduced. After the PMMA patterns with

modified size are acquired, chromium layer wet etching is carried out to transfer the modified pattern size into chromium layer. By SiO_2 dry etching with the chromium mask, SiO_2 nanoimprint mold with modified feature size is fabricated. Illustrated as Figure 10 (right) annealed PMMA patterns are directly employed as the SiO_2 etching mask. Although PMMA is not an ideal mask material for CHF_3 etching due to its low etching selectivity over SiO_2 (which is about 1:1 according to our experiments), compared with Cr, we simplified the fabrication process by removing the Cr wet etching step and the outcome of SiO_2 dry etching was also acceptable which will be demonstrated later.

Experimentally, 36 nm chromium layer was evaporated onto SiO_2 substrate by thermal evaporation. 2 wt% PMMA (M_w=15k) in toluene solution was spin-coated on the chromium layer at the speed of 4000 rpm for 30 seconds. PMMA layer with a thickness of 76 nm was obtained. A SiO_2 mold with 350 nm square array pattern was used to carry out nanoimprint at 175 ^{o}C at 5 MPa pressure. After residual layer removal by oxygen RIE, isolated PMMA pillars were annealed at 150 ^{o}C for various time periods. Then chromium wet etching and SiO_2 RIE were applied to accomplish the pattern transfer from PMMA to SiO_2. In Figure 11, the original PMMA patterns (Figure 11 (a)) with 350 nm feature size are compared with modified chromium patterns (Figure 11 (c)). The modified chromium patterns were achieved by annealing the original PMMA patterns at 150 ^{o}C for 150 seconds, followed by chromium wet etching. Sub-100 nm spacing can be observed compared with original 350 nm, which is more than 70% reduction and the modified pattern size can be well controlled by annealing temperature and time.

Modified spacing between chromium nanodots at 150 ^{o}C for various annealing time is summarized in Table 1.

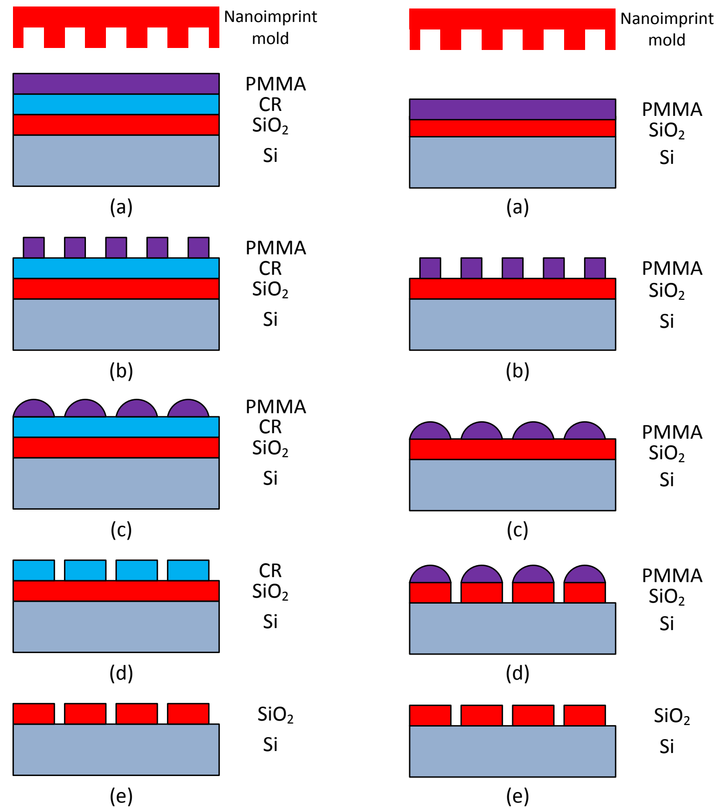

Figure 10. Fabrication procedure of nanoimprint mold with reduced feature size by PMMA controlled reflow. Left: Schematics of polymer pattern modification by controlled polymer wetting: (a) sample prepared by Cr evaporation and PMMA spin-coating; (b) PMMA patterning by nanoimprinting and oxygen RIE; (c) PMMA re-patterning by thermal annealing; (d) Cr wet etching with PMMA mask, which is then removed by acetone; (e) SiO_2 dry etching by CHF_3 RIE with Cr mask, followed by Cr removal. Right: (a) sample prepared by Cr evaporation and PMMA spin-coating; (b) PMMA patterning by nanoimprinting and oxygen RIE; (c) PMMA re-patterning by thermal annealing; (d) SiO_2 dry etching by CHF_3 RIE with PMMA mask; (e) PMMA mask removal by acetone.

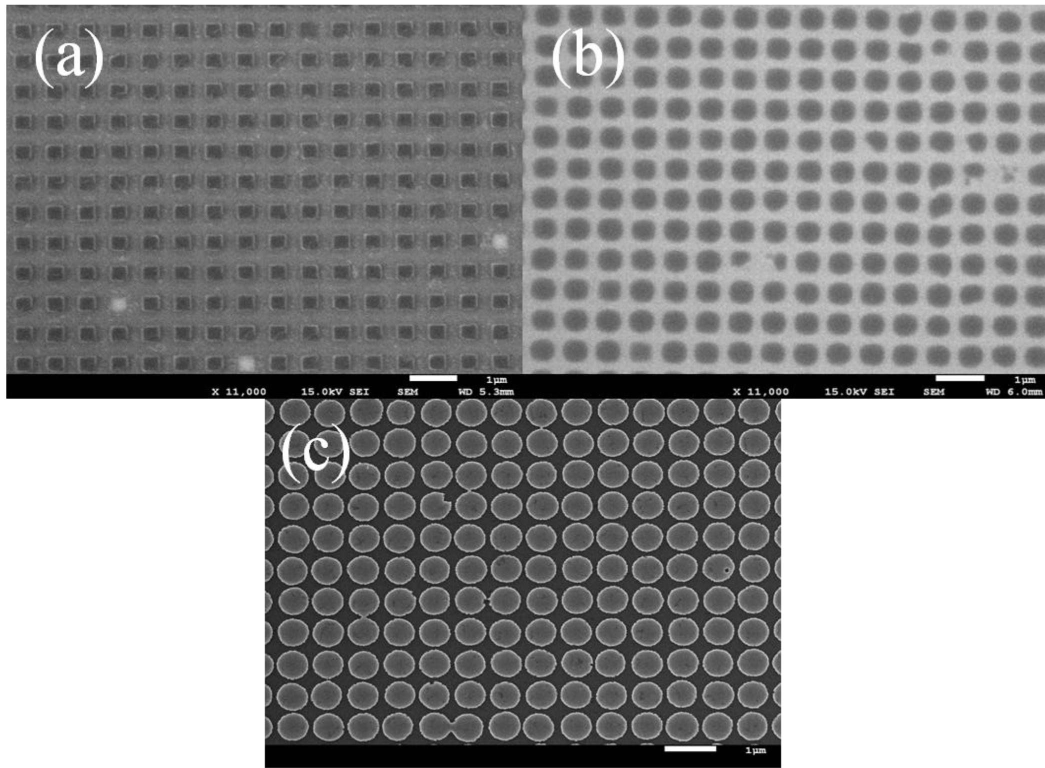

Figure 11. (a) Original PMMA square array pattern formed by nanoimprint; residue layer was removed; the spacing between two square is c.a. 350 nm; (b) modified PMMA patterns by thermal annealing at 150oC for 150 seconds; (c) chromium patterns obtained from (b) by chemical wet etch; the spacing between two dots is c.a. 80 nm.

Table 1. Modified pattern spacing at 150 ^{o}C.

Annealing time (second)	Minimum pattern spacing (nm)	Reduction percentage
0	350	0%
60	270±10	(23±3)%
120	141±10	(60±3)%
150	83±6	(76±2)%

For the alternative process shown in Figure 10 on the right, we moved to grating patterns to demonstrate our method. Experimentally 200nm PMMA layer was deposited on SiO_2 substrate by 5wt% 15K PMMA in toluene solution spin-coating for 30 seconds at 4000 rpm. Then nanoimprint lithography was applied at 175℃ and 5Mpa, followed by oxygen RIE to remove residual layer. Isolated PMMA patterns were then annealed at 120℃ for various time periods. Then with annealed PMMA patterns as the etching mask, SiO_2 dry etch was applied for 10 minutes, resulting in trench depth of 120 nm. PMMA etching mask was then removed by acetone and SiO_2 gratings with modified feature sizes could be obtained. In Figure 12(a), 350 nm gratings mold was used as the initial mold and by process in Figure 10 ((a)-(e), right) we fabricated modified nanomprint mold with duty cycle of 77% (Figure 12(b)).

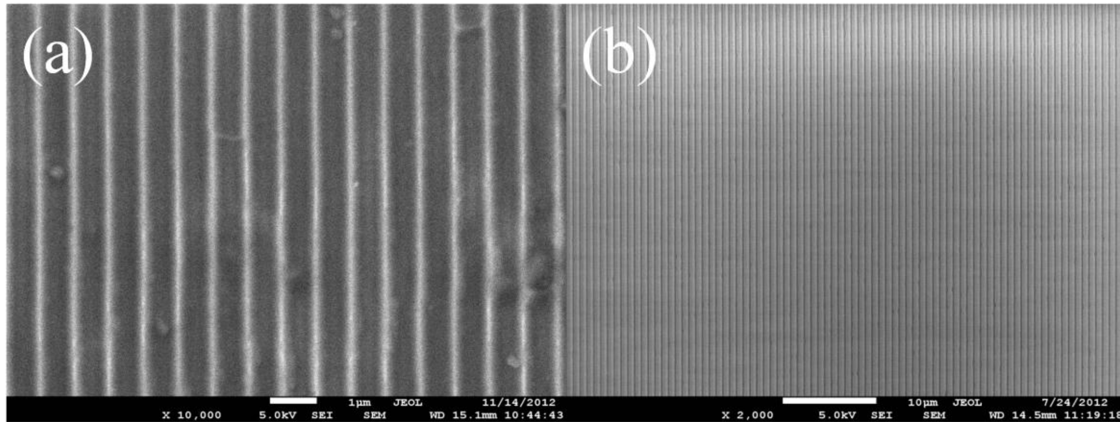

Figure 12. (a) Original 350 nm gratings nanoimprinting mold with duty cycle of 50%; and (b) modified SiO2 gratings with duty cycle of 77%.

2.3.2 Discussion

In this section we investigated the reflow of PMMA patterns by thermal annealing above T_g, the minimum feature size can be reduced significantly up to 76% with 350 nm grids structure and half-pitch grating. This technique is promising for sub-10 nm fabrication if patterns with smaller dimension are used. However due to the limitation of our facility currently we are not able to achieve sub-10 nm resolution. Besides the non-uniformity of the reflow process of different patterns and merging of adjacent patterns are both of concern. Another technique regarding these issues will be addressed in the following section.

2.4 Controlled reflow based on exceptional thermal stability of polycarbonate

Thermoplastic polymer micro- and nanostructures patterned by nanoimprint suffer pattern decay when heated to a temperature close to or above the polymer's glass

transition temperature, such as PMMA resist as we discussed in the previous section. In this section, we report unexpected thermal stability of polycarbonate nanostructures at temperatures well above its glass transition temperature. Based on this observation, we develop a unique technique for high resolution polymer patterning by determining the "end point" of polymer reflows. This technique is characterized as the precise control of polymer reflows regardless of annealing time, which avoids the time-domain nonlinear reflow of polymer. Since thin and ultrathin polymer film is incorporated with lithography technique and devices, this technique is expected to find applications in various fields.

2.4.1 Motivation

Thermal nanoimprint is a physical molding process to replicate nanoscale patterns from a hard template to soft materials. One of the challenges is the pattern stability issue for thermal NIL. In thermal NIL, thermoplastic polymers are shaped into patterns by polymer flow under pressure at a temperature above the glass transition temperature (T_g) of the polymer. It is well known that nanoimprinted thermoplastic polymer micro- and nanostructures are not stable and pattern decay due to internal stress relaxation can occur at a temperature close to or even below the polymer's T_g [11]. Such thermo instability negatively impacts the applications of thermoplastic polymer micro- and nanostructures patterned by NIL. The thermal-annealing-induced reflow behavior of polymer patterns fabricated by thermal NIL has been widely investigated.[12, 13] In general, dramatic thermal expansion can be observed by thermal annealing of the polymer patterns at

temperatures above T_g, and with extended annealing the pattern shape cannot be recognized any more. In this work, we report that shallow nanostructures of thermoplastic polycarbonate have exceptional thermal stability on both chromium and SiO_2 substrates even at temperatures well above the T_g of polycarbonate. First we observed and examined the thermal stability of sub-50 nm polycarbonate pillars on chromium layer by thermal annealing at temperatures from T_g (150 ^{o}C) up to T_g+150°C and the statistical data regarding the pattern dimension was provided. In addition, we investigated the reflow behavior of polycarbonate gratings with thickness above 50 nm. Although pattern relaxation was observed at the initial stage of the thermal annealing, stable polycarbonate gratings patterns were obtained after reaching the "end point" of the polymer reflows, resulting in a trench with reduced width, depending on the initial thickness of the gratings, between two gratings. One application of the thermal stability of shallow polymer micro- and nanostructure is to determine the end point for polymer reflows for high resolution polymer patterning by careful control of the pattern thickness prior to the thermal annealing. In this work we started with grating patterns of 700 nm pitch (50% duty cycle) and achieved a minimum trench size of 35 nm by this technique. Moreover, the modified polymer features can be transferred into the underlying SiO_2 substrate for further application.

2.4.2 Experimental details

Two types of NIL molds were prepared in this work. A Si mold with array of holes (50 nm diameter, 100 nm pitch size and 100 nm depth) was used to examine the exceptional

thermal stability of polycarbonate pillars at sub-50 nm scale. A 700 nm period (50% duty cycle) SiO_2 mold with 250 nm depth was used to carry out a serial of experiments to investigate the end point of polymer reflows with respect to the initial thickness of the patterns. Those two molds were fabricated by electron beam lithography and dry etch. Both the molds were coated with 1H,1H,2H,2H-perfluorodecyltrichlorosilane (FDTS) as a hydrophobic surfactant for mold release. Polymer resist used in this work is polycarbonate resin (secondary standard, Scientific Polymer Product, Inc.) with average molecular weight of 36600. 1 wt% and 4 wt% polycarbonate solution were prepared by dissolving polycarbonate powders into cyclohexane solvent. Polycarbonate thin film was obtained by spin-coating on SiO_2 substrate or 40 nm chromium layer, which was thermally evaporated onto Si wafer. After spin-coating, samples were placed on a hotplate to remove the residue solvent. The thickness of the polycarbonate thin film was measured by Nanofilm EP3-SE ellipometer.

We experimentally examined the thermal stability of polycarbonate pillars of sub-50 nm in size. The sample was prepared by spin-coating of 50 nm polycarbonate on 40 nm chromium layer. Polycarbonate resist (T_g=150 ^oC) was imprinted by Si mold with holes of 50 nm in diameter and 100 nm in depth at 220 ^oC and 5 MPa. Oxygen RIE was applied to remove the residual layer and to control the final height of the pillar patterns. The height of the pillars was around 35 nm. The polycarbonate pillar patterns were annealed at elevated temperatures from 150 ^oC up to 300 ^oC, which is well above its T_g,

for various time periods. The pattern morphology was characterized by JEOL JSM-7500F SEM.

For polycarbonate gratings with thickness above 50 nm, we found that although the patterns spread on the substrate at the early stage by thermal annealing, they finally ended up with stable structures without further reflow regardless of annealing time. The final pattern size after the reflow can be determined by the initial height of the polycarbonate gratings. Figure 1illustrates the schematics of this technique. Polycarbonate resist is patterned by thermal NIL on SiO_2 or chromium layer and the grating height is controlled by oxygen RIE. (Figure 13 (a)) Then the assembly is heated on a hotplate for polymer reflow. (Figure 13 (b)) The stable structures are formed in short time and free of deformation regardless the annealing time (Figure 13 (c)). In order to justify this technique, polycarbonate film was prepared by spin-coating on SiO2. Then polycarbonate resist was imprinted by 700 nm period (50% duty cycle) SiO_2 mold with 250 nm depth. The residue layer was removed and the final height of the gratings was controlled by oxygen RIE. Then thermal annealing was carried out at 200 ^{o}C for 30 min. After nanoimprint and thermal annealing, the modified polymer patterns were transferred into SiO_2 by CHF_3 RIE. The pattern morphology was characterized by JEOL JSM-7500F SEM. Similar process was also done for polycarbonate film on 40 nm chromium layer which was thermally evaporated on Si wafer.

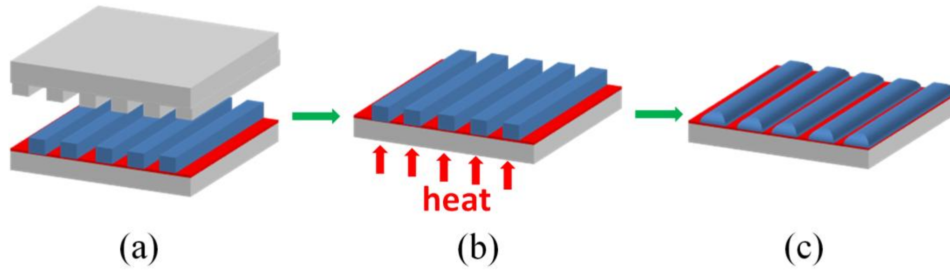

Figure 13. A schematic of (a) polycarbonate resist patterned by NIL on chromium layer and grating height controlled by oxygen RIE; (b) sample annealed on hotplate at elevated temperature and (c) stable structures formed by polymer reflows regardless of annealing time.

2.4.3 Exceptional thermal stability of sub-50 nm polycarbonate pillars

In order to investigate the thermal stability of sub-50 nm polycarbonate pillars, we annealed the sample prepared in 2.2 at 300 ^{o}C for 5 min, 10 min, 20 min and 30min (Figure 14). The corresponding statistical data of the pillar diameter from a random area was obtained by SEM and analyzed using ImageJ (Figure 15). It is clearly observed that the polycarbonate patterns exhibited unusual stability at temperatures well above its T_g. Only the diameter distribution information of 30 min sample is presented here, since the all scenarios for 5 min, 10 min and 20 min samples are identical, which implies the rapid formation of stable structures. In addition, polycarbonate pillar stability within broader temperature range from T_g (150 ^{o}C) to T_g+150 ^{o}C (300 ^{o}C) was also tested, which produced similar results. For the same polycarbonate pillars with a height much greater than 50 nm, we observed significant diameter increase due to pattern relaxation. The

polymer melts spreading on a certain substrate is complicated. The polymer-substrate interaction and the stretching of entangled polymer chain have to be accounted at the same time. First, the interaction between the polymer chain and the substrate may result in a significant mobility difference between the bulk and interface [14, 15]. It has been reported that a substantially decreased chain mobility is found in ultrathin polymer film with the thickness less than 150 nm [16]. Second, as the polymer film thickness deceases on the order of the radius of gyration (R_g), the polymer chains have to stretch in order to spread on the surface for entangled polymer. In this case, the free energy for chains deformation needs to be considered. Zhao et al. [17]reported that polyethylene propylene film with less than 10 nm thick could not completely wet the native-oxide-covered Si substrate due to the entanglement of polymer chains. Given the facts that the polycarbonate pillars in our work can be considered as melts with relatively low viscosity at 300 ^{o}C [18] and the thickness of the pillars is around 35 nm, which is only several times of R_g, the exceptional thermal stability can be ascribed to strong chain entanglement. However, the details regarding the polymer dynamics need further study and this issue will be further discussed in chapter Ⅲ.

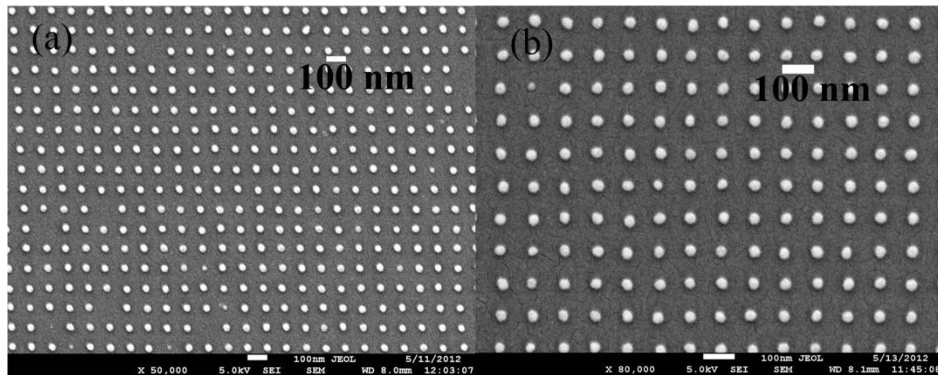

Figure 14. (a) polycarbonate pillars without thermal annealing and (b) polycarbonate pillars with 300 °C thermal annealing for 30 min.

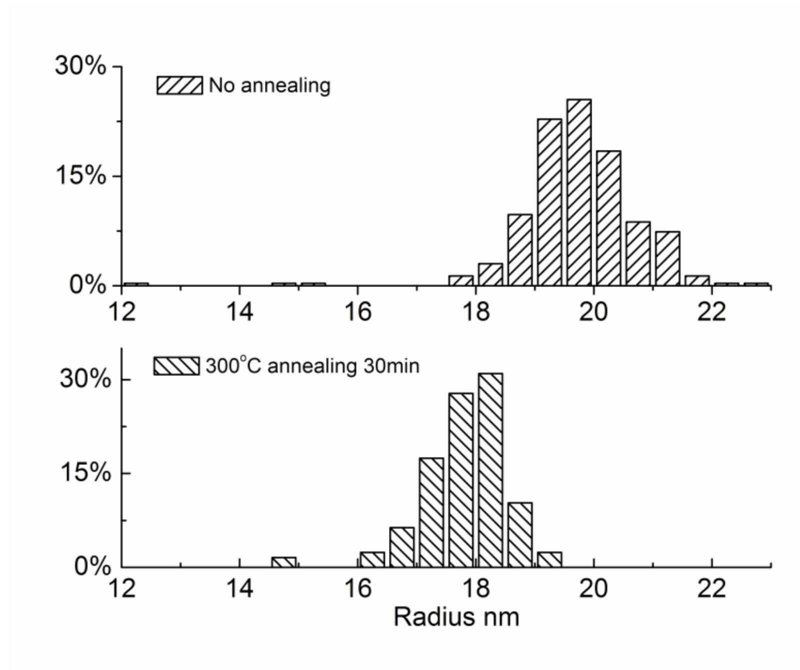

Figure 15. Statistical distribution of polycarbonate pillar radius: no annealing on the top and 30 min 300 °C annealing on the bottom.

2.4.4 Polymer reflow end point of polycarbonate gratings

As is discovered that the polycarbonate gratings with thickness more than 50 nm ended up with stable structures by thermal annealing despite initial reflow, we utilized this phenomenon as a nano-patterning technique and justified this technique by the following tests. The polycarbonate gratings were fabricated as described in 2.3.2 on SiO_2 substrate and the height of the pattern was controlled to be 150 nm and 70 nm by oxygen RIE. Samples were placed on hotplate at 200 ^{o}C for 30 min to allow polymer reflow and the formation of stable structures. The grating gap size shrinkage after the thermal annealing can be observed from Figure 16 (a) to (b). The annealed polymer grating features can be transferred into SiO_2 layer by CHF_3 RIE. SiO_2 gratings in Figure 16 (c) were obtained by RIE from (b) with the initial height of 150 nm (Figure 16 (a)). While in Figure 16 (d) SiO_2 gratings with a larger gap size resulted from a smaller initial height (ca. 75nm).

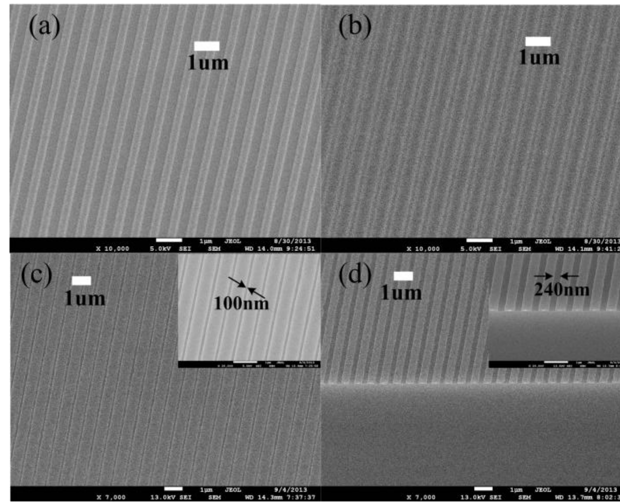

Figure 16. (a) polycarbonate gratings (700nm pitch, 50% duty cycle and ca.150 nm height) fabricated by thermal NIL and oxygen RIE; (b) polycarbonate gratings after thermal annealing at 200 ^{o}C for 30 min; (c) SiO_2 gratings by CHF_3 RIE from (b); and (d) SiO_2 gratings by CHF_3 RIE from polycarbonate gratings with ca.70 nm height. Inserts are at higher magnification.

The trench widths after thermal annealing depend on the initial thickness of the polycarbonate gratings, which can be controlled by the oxygen RIE time. The smaller trench size is expected from thicker gratings; however at the same time partial or complete merge can happen if the gratings are too high. We designed a serial of experiments to implement this technique. SiO_2 grating mold with 700 nm pitch and 50% duty cycle was used to pattern polycarbonate resist by thermal NIL and the grating thickness of the patterns was controlled by RIE time. We prepared several sets of samples with individual grating thickness and annealed the samples at 200 °C for 30 min. The height information of the grating patterns was acquired by Bruker Dimension Icon AFM and the pattern feature size after thermal annealing was characterized by JEOL

JSM-7500F SEM. The plot in Figure 17 illustrates the how the trench sizes of the gratings after thermal annealing are related to the initial thickness. Based on this observation, the increasing initial thickness will result in shrinking trench sizes and this could be employed for high resolution polymer patterning. Figure 18 shows the minimum trench size of 35.0±5.2 nm we achieved, which is a 90% reduction of the original feature size, by careful control of RIE processing time and the initial thickness was estimated to be 200 nm based on the initial pattern thickness, etching time and etching rate. The grating edge roughness was originated from side etch of the oxygen RIE process. For nanofabrication application, the modified polymer pattern can be easily transferred to the underneath chromium layer by wet etch.

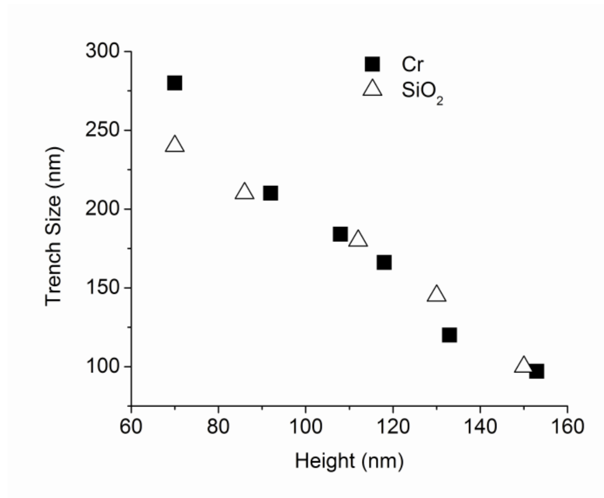

Figure 17. The plot of trench sizes after thermal annealing on chromium (square) and SiO_2 (triangle) substrate as a function of the initial height of the grating before thermal annealing.

It has been demonstrated that a transition from high rate pattern size evolution at early stage to a reduced rate exists when the polymer patterns are annealed above T_g [11, 19]. For the technique we presented in this paper, rapid formation of stable structures is essential for feasibility and high throughput. In order to investigate the evolution of the polycarbonate grating by thermal annealing, we characterized the pattern morphology by examining the trench size at different time segments. Polycarbonate resist was imprinted by 700 nm pitch (50% duty cycle and 250 nm depth) SiO_2 grating mold. The grating height was controlled to be 70 nm by oxygen RIE. After that the sample was annealed at 200 ^{o}C on hot plate and the trench size was measured by SEM at 5 min, 10 min, 20min, 30 min and 60 min during the annealing process. The corresponding information is shown in Figure 19. It indicates that the stable structures are formed within 5 min and remain unchanged in long time regimes.

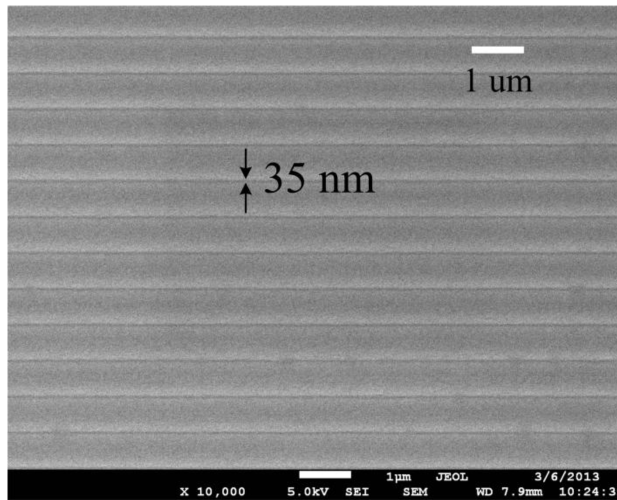

Figure 18. Polycarbonate gratings with trench size of 35.0±5.2 nm after thermal annealing.

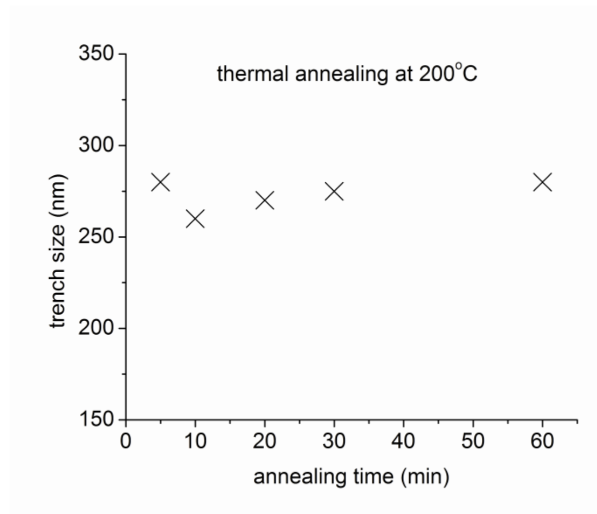

Figure 19. The plot of trench sizes with respect to the annealing time. The initial height for the grating patterns before annealing is 70 nm.

2.4.5 Summary

In summary, we have discovered the exceptional thermal stability of polycarbonate nano-pillars on both chromium and SiO_2 layer at temperatures well above its glass transition temperature (T_g) and developed a technique for high-resolution polymer patterning by determining the “end point” for polymer reflows, combined with nanoimprint lithography. In the first part of this work, we examined the thermal stability of polycarbonate pillars at sub-50 nm scale and statistical data of the dimension information showed that the nano-structures could maintain their original morphology at temperatures well above T_g. For polycarbonate gratings above 50 nm, it was observed that the formation of stable structures was followed by a rapid reflow at the early stage and the trench size between the gratings was determined by the initial grating thickness before thermal annealing regardless of annealing time. In the second half of this work, we employed this phenomenon for high resolution polymer patterning. Reduced feature sizes, depending on the initial thickness, were obtained by thermal annealing and trenches down to 35 nm wide were achieved by carful control of RIE time. The modified features could be easily transferred to the underneath chromium layer by wet etch for patterning applications. SiO_2 gratings with reduced feature sizes were obtained by similar process. Moreover, given the stability issue for thermoplastic polymer patterns at temperatures close or above T_g, this technique opens up a great possibility for step-and-repeat thermal nanoimprint[20]. This topic will be presented in the following chapter.

CHAPTER III

STEP-AND-REPEAT THERMAL NANOIMPRINT

A key issue that limits the application of thermal nanoimprint towards large scale commercial nanofabrication is the low throughput. As we discussed in the introduction chapter, the throughput of thermal nanoimprint is hindered by heating and cooling cycle of the thermal plastic resist. On one hand, the imprinting resist needs to be heated to temperature well above the glass transition temperature (T_g) so that the resist can be well patterned with low viscosity. On the other hand, after imprint process, temperature well below T_g is required before mold release in order to avoid pattern deformation. Therefore the throughput of thermal nanoimprint can be severely limited by the temperature control process. Moreover, for traditional thermal nanoimprint, only a single imprinting process can be implemented with a substrate due to the temperature cycling issue. That is, if multiple thermal imprints are to be done with the same substrate, the previously defined patterns could be significantly degraded due to high temperature annealing. Compared with traditional thermal nanoimprint, UV nanoimprint is preferred for large-scale high-throughput manufacturing. In addition, UV nanoimprint can be implemented in a step-and-repeat fashion, especially known as Step-and-Flash Imprint Lithography (SFIL)[21-24], which can further improve the throughput. In this chapter, we will start with the endeavor to boost the throughput of traditional thermal nanoimprint. Then we will present step-and-repeat thermal nanoimprint based on the exceptional thermal stability of polymer resist. In the end of this chapter, potential of this technique

is discussed. We ascribe the thermal stability of polymer resist to the polymer chain entanglement.

3.1 Introduction to step-and-repeat nanoimprint

High throughput is demanded for commercial nano-fabrication and photolithography has been the dominating technique for large scale manufacturing, where projection lithography incorporated with stepper is widely used. For UV nanoimprint, Step-and-Flash Imprint Lithography[21] invented by Molecular Imprint is featured by high resolution as well as high throughput. The process is operated in a step-and-repeat fashion which is similar to the stepper. The imprint process within every single cell is similar to the UV nanoimprint presented in the introduction chapter and multiple imprints are implemented by local UV curable solution dispense and wafer stage displacement. Such step-and-repeat fashion cannot be directly applied to thermal nanoimprint because the heating of thermal plastic resist will dramatically damage the previous imprinted patterns. In order to overcome this issue, efforts have been made by researchers with varieties of methods.

One method to circumvent the damage caused by high temperature annealing to the previous imprinted resist is to heat the imprint mold instead of the whole substrate. Commercial nanoimprint tools such as NPS300 nanoimprint stepper could operate the process in a step-and-repeat fashion based on the temperature control with the mold instead of the whole substrate. Researchers[25, 26] have reported sequential thermal

nanoimprint on the same substrate based on such tools. However the cycling process of heating up above T_g and cooling down below T_g are still necessary for reliable pattern definition, which is one of the issues limiting the throughput as we discussed. Yoon[27] et al. reported a technique to operate thermal nanoimprint with step-and-repeat fashion. In their work, the imprinting stacking is heated as a whole by IR lamp. However a metal screen is placed between the lamp and the resist where is not patterned. Heating is blocked from the shaded area by the metal screen. And after every single imprint, the defined patterns need to be shaded by the metal screen to avoid further thermal annealing. Although they claim that it takes only a few minutes for cooling down by using the IR lamp as the heating source, the heating and cooling cycle is still inevitable in their technique. In addition, the feasibility of placing metal screen in between is also of concern without detailed information.

Room temperature nanoimprint is another method to avoid high temperature during the imprint procedure. This technique can be based on the free volume compression of amorphous polymers under high pressure[28]. PMMA micro-channel fabricated by room temperature has been reported[29]. However imprint pressure up to 2700 psi was used compared to a typical pressure of 700 psi performed in high temperature thermal nanoimprint. The poor thermal stability of polymer patterned by high pressure at room temperature could be a concern due to the free volume restoration and the incomplete patterning due to limited free volume within the polymer resist can cause problems, as is reported that the depth of the micro-channel depends on the pressure applied[29]. Room

temperature nanoimprint in a step-and-flash fashion and multiple imprints at the same location have been reported[28, 30]. In addition, room temperature nanoimprint was also performed based on solvent damping[31] and plasticizing[32]. However these techniques are not available for step-and-repeat fashion since the exposure towards solvent can cause pattern decay.

In this chapter we will present a unique technique to implement thermal nanoimprint in a step-and-repeat fashion. As we discussed in the previous chapter, ending point of polymer grating reflow under thermal annealing is observed for polycarbonate patterns. Larger trench size, which means less polymer reflow, is obtained with thinner polymer patterns. Therefore, we expect negligible pattern deformation as the thickness of the polymer resist is controlled to be extremely thin. The exceptional thermal stability of polycarbonate is ascribed to the polymer chain entanglement and the experiment details are addressed in the following section.

3.2 Step-and-repeat thermal nanoimprint

Based on the thermal stability of shallow polycarbonate structures, the step-and-repeat process for thermal nanoimprint lithography was tested in the following methods. Polycarbonate thin films, with the thickness of 90 nm, 40 nm and 20 nm, were prepared on 40 nm chromium layer on top of Si wafer by spin-coating. Then the polycarbonate resist was imprinted at T_g (150°C) and 5 MPa for 5 min; after that the mold was released from the substrate immediately without cooling down and relocated at the adjacent

region for another imprinting process. Figure 20 shows a substrate with two imprinted pads. In order to verify our technique at elevated temperature, we conducted the same process with 20 nm polycarbonate resist at 200°C, which is identical to conventional thermal nanoimprint. A 700 nm period (50% duty cycle) SiO_2 mold with 250 nm depth was used. The pattern morphology was characterized by JEOL JSM-7500F SEM and Bruker Dimension Icon AFM.

Figure 20. Photography of a substrate imprinted by two sequential steps of step-and-repeat process.

For polycarbonate resist of 90 nm, 40 nm and 20 nm thick, two adjacent regions, which are illustrated in Figure 20, were successfully imprinted by step-and-repeat process. However the dimensions of the fabricated features highly depend on the resist thickness and the related thermal stability and reflow behavior. For the 90 nm thick resist at 150°C step-and-repeat NIL, the grating height formed by 700 nm pitch (50% duty cycle and 250 nm depth) SiO_2 grating mold is expected to be around 180 nm and the trench size ended up with around 250 nm, which means the corresponding ridge size is around 450 nm. And meanwhile around 300 nm trench size was obtained for 40 nm resist. For 20 nm resist, the expected grating height was 40 nm and features at this scale range are anticipated to be extremely stable based on our observation in chapter Ⅱ. And the imprinted patterns with 350 nm trench and 350 nm ridge, which is identical to original mold, solidify our conclusion at both 150°C and 200°C. The SEM images of the imprinting serials are shown in Figure 21.

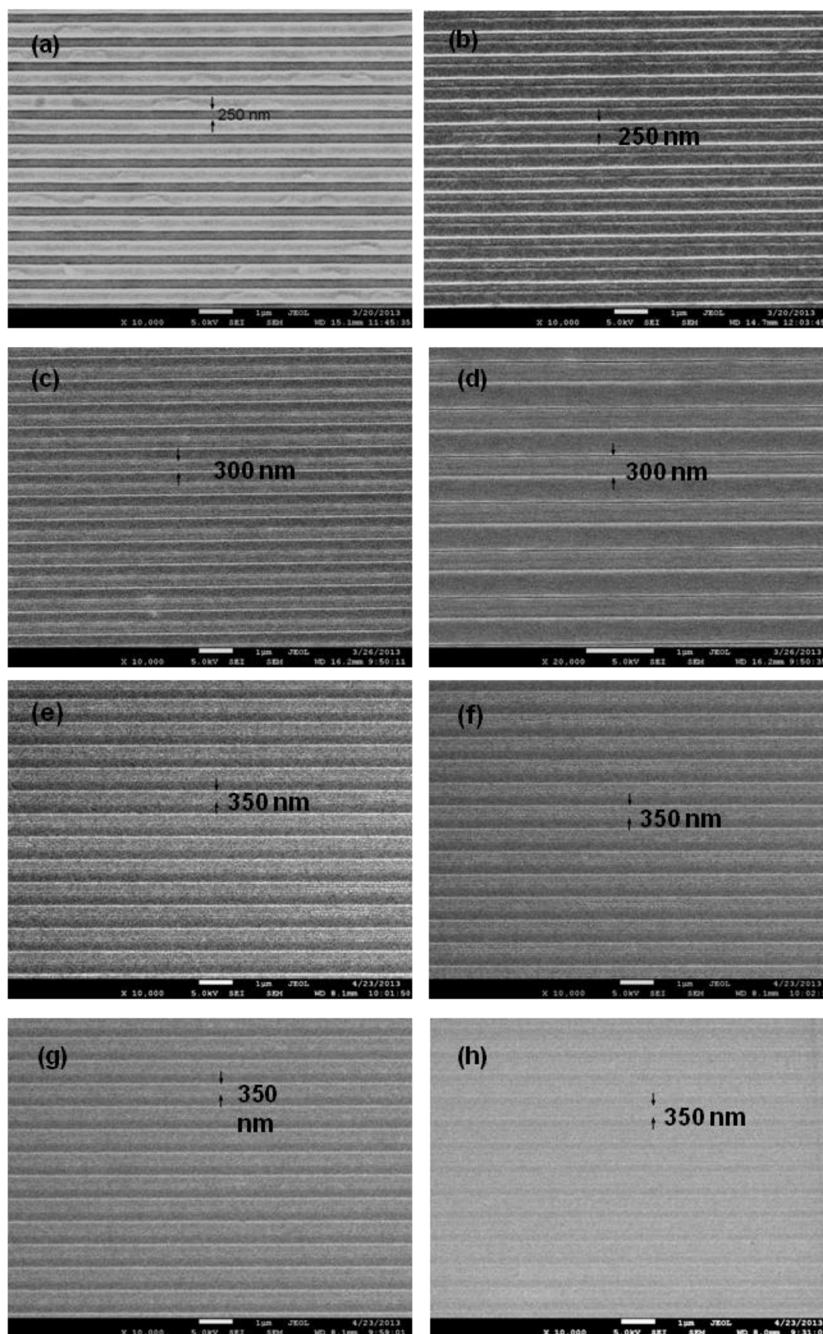

Figure 21. Trench size of grating structures fabricated by two sequential nanoimprint steps by step-and-repeat process: 90 nm resist imprinted at 150 ^{o}C with (a) step 1 and (b) step 2; 40 nm resist imprinted at 150 ^{o}C with (c) step 1 and (d) step 2; 20 nm resist imprinted at 150 ^{o}C with (e) step 1 and (f) step 2; 20 nm resist imprinted at 200 ^{o}C with (g) step 1 and (h) step 2.

The effect of different substrates was also investigated as the interaction between the polymer and substrate may play a role in the reflow dynamics[15, 33]. 20 nm polycarbonate (M_w=36k) was prepared on 100nm SiO2 substrate by spin-coating 1 wt% polycarbonate cyclohexane solution at 4000 rpm for 1min. The samples were annealed on hotplate at 100°C to remove the residue solvent. After that, step-and-repeat thermal nanoimprint was operated at 200°C under 5 MPa for 5 min. The nanoimprint mold (700 nm pitch, 50% duty cycle and 250 nm depth) was released and moved to the adjacent region immediately after the previous imprint without the cooling process. Two imprints were carried out on the same substrate and the polymer patterns were characterized by Bruker Dimension Icon AFM (Figure 22). The same process could also be complete for polycarbonate resist (M_w=36K) on 100nm gold surface, which was evaporated onto a Si wafer. Based on the experiments of step-and-repeat thermal nanoimprint on SiO_2, Cr and Au, we found no obvious evidence that the interactions between the polymer resist and the substrate could significantly impact the reflow behavior for patterns with extremely small thickness (c.a. 40 nm from Figure 22). Although different macro equilibrium state for PDMS droplet spreading was reported on high-energy and low-energy surface, which was ascribed to hydrogen bonding between the material and substrate[15, 33-36]. Rather than the material and substrate interaction, we believe that the property of polymer thin film itself is the dominating factor that accounts for the exceptional polymer thermal stability.

In addition to the step-and-repeat process, we also present the potential of multiple imprinting based on the thermal stability of polycarbonate resist. In our experiment,

gratings patterns were produced during the first imprinting step and without cooling down; the grating mold was removed and immediately pressed on top of the grating patterns formed in the first step, but in the orthogonal direction. The pattern morphology was characterized by JEOL JSM-7500F SEM. Figure 23 presented the grids structures fabricated by a dual imprint at orthogonal directions. The second imprint was applied after the mold separation of the first imprint without cooling down. Despite of another imprint, the grating segments which were not pressed during the second NIL suffered no damage.

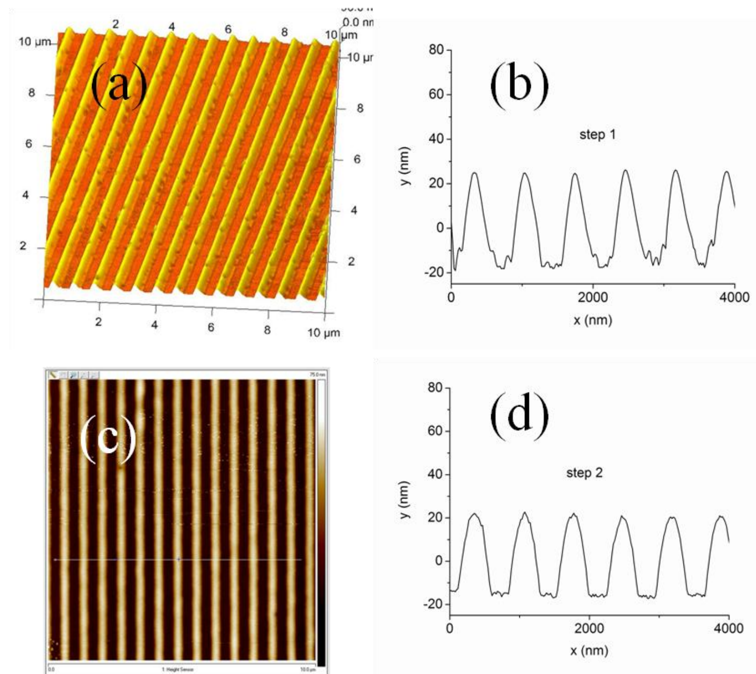

Figure 22. AFM profile of step-and-repeat thermal nanoimprint of 20 nm polycarbonate resist: profile of step 1 (a) and section information (b); profile of step 2 (c) and section information (d).

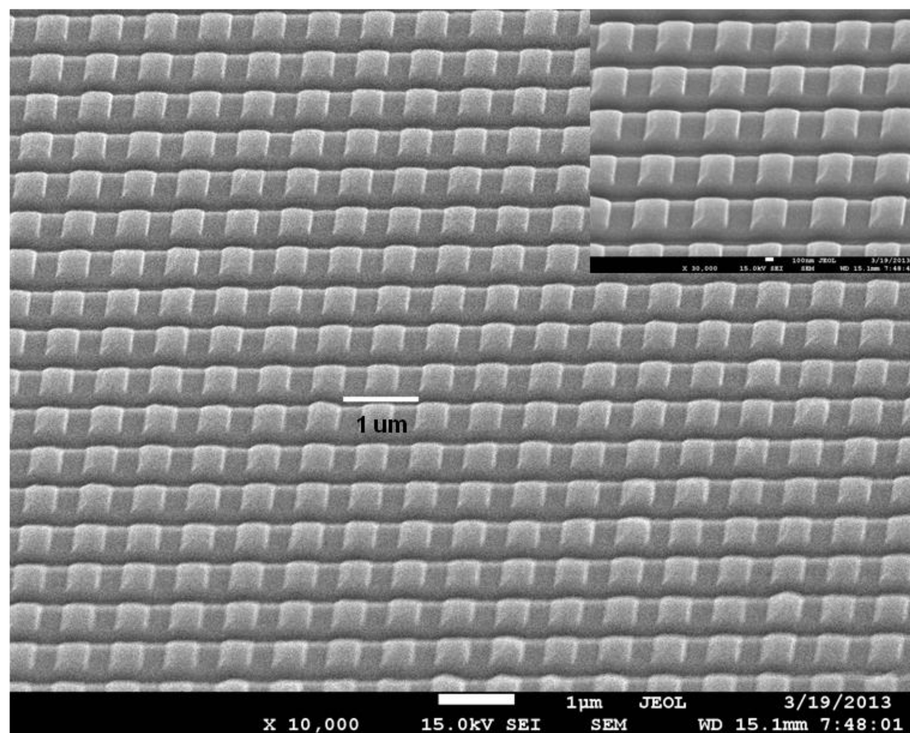

Figure 23. Grid structures fabricated by dual nanoimprint of step-and-repeat process at orthogonal directions on 90 nm polycarbonate resist; inserts are at higher magnitude.

3.3 Polymer chain entanglement

The origin of exceptional thermal stability of polymer patterns can vary. Enhanced crystallization of polycarbonate[37] and controlled crystallization induced by nanoimprint lithography[38, 39] have been reported previously. Since the polymer melting temperature can be dramatically increased with the transition from amorphous to crystalline state, we investigated the possible crystallization of polycarbonate resist during step-and-repeat thermal nanoimprint. 20 nm polycarbonate (M_w=36k) film on Si wafer was prepared by spin-coating and then the resist film was nanoimprinted at 200°C for 5 min. The mold

was released immediately after imprint without cooling down. Both the resist film and the imprinted sample were characterized by x-ray diffraction. Figure 24 shows the x-ray diffraction spectrum of 20 nm polycarbonate resist spin-coated on Si wafer and after step-and-repeat thermal NIL. By comparing the spectrum we do not observe obvious crystalline peak after nanoimprint. And the possible crystallization induced by spin-coating is also excluded. Given that the crystallization process of polycarbonate is extremely slow—crystallization half-time up to 9 hours at 190°C[40, 41]—it could not be accounted for our observation. In addition, the material and substrate interaction may not be the primary reason as we discussed in the previous section. Polymer chain alignment induced during thermal nanoimprint could be another possible contributor however Raman spectrum provided no evidence based on our experiment.

The potential of step-and-repeat thermal nanoimprint could be ascribed to the polymer chain entanglement of polycarbonate resist. For low molecular weight polymers, the polymer melts dynamics is described by Rouse model. In Rouse model[42], the polymer chain is described as beads, which are submolecules larger than monomer, connected by springs in a stochastic background . This model is developed based on an isolated polymer chain and suit low molecular weight polymer and low concentration solution very well. Predicted by Rouse model the self-diffusion coefficient is $D \propto N^{-1}$and the viscosity $\eta \propto N$, where N is the degree of polymerization.

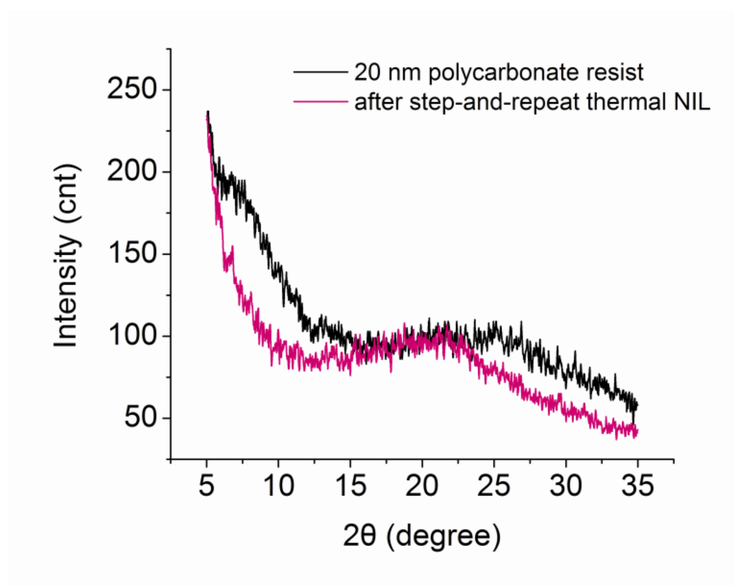

Figure 24. X-ray diffraction spectrum of 20 nm polycarbonate resist spin-coated on Si wafer (black) and after step-and-repeat thermal NIL (purple).

For polymer with very high molecular weight, the dynamics of polymer melts are found to be quite different from that of low molecular weight polymers. The interpenetrating of polymer chains limits the diffusion of a single chain towards the lateral direction of its backbone, as the chain movement can drag other entangling chains where large friction can be resulted from. The polymer chain entanglement is described by the reptation model. In the reptation model, a single chain is confined within a tube surrounded by other chains. $D \propto N^{-2}$ and $\eta \propto N^{-3.4}$ have been reported from references[43, 44]. The entanglement chain length N_e is defined in such a way that for a given polymer if $N<N_e$ the Rouse model dominates while if $N>N_e$ the reptation model overtakes the Rouse model. For a specific polymer, the entangled molecular weight M_e is given as $M_e=m*N_e$, where m represents the molecular weight of a monomer. If $M_w>M_e$, the dynamics of the

polymer melts can be described by reptation model and larger M_w is, the more entangled the network is expected. In order to test feasibility of thermal step-and-repeat nanoimprint towards polymers with different entanglement molecular weight, we selected poly (methyl methacrylate) (PMMA, M_w=15k), polystyrene (M_w= 35k) and polycarbonate (M_w=36.6k), as we used previously, to be the imprint resist. Thermal step-and-repeat nanoimprint was performed at temperatures 50°C above the T_g of corresponding materials (150°C for PMMA, 200°C for polycarbonate and 150°C for polystyrene). The entanglement molecular weight of polymers has been reported experimentally and theoretically[45, 46]. From the tabular values we pick up the entanglement molecular weights: c.a.10k for PMMA, c.a. 13k for polystyrene and c.a. 1K for polycarbonate, which renders 1.5 M_e, 2.8 M_e and 36 M_e for the resist of PMMA, polystyrene and polycarbonate. On the other hand, the experiments supported our extrapolation very well. Only polycarbonate resist is available for thermal step-and-repeat nanoimprint with extremely entangled network while the patterns suffered severe decay for PMMA and polystyrene.

The polymer reflow "ending point" and the exceptional thermal stability of polycarbonate patterns can be ascribed to the chain entanglement in polymer thin films. The wetting behavior of polymer melts has been widely investigated[35, 47]. For high energy substrates such as SiO_2, they are usually wettable to most polymer melts or relatively thick polymer film. Total wetting can take place if the critical surface tension of the substrate is larger than the surface tension of the polymer melts [48]. However if the

polymer film thickness is reduced to be on the order of R_g, the polymer chains need to stretch themselves in order to wet the substrate. If the polymer is in entanglement region, the energy required to stretch the chains will be dominating and total wetting is more unlikely to happen. Zhao[49] et al. reported the wetting properties of liquid PEP on native SiO_2 and HF-etched Si substrate. They observed that dewetting occurs when the PEP film thickness is smaller than its R_g, and by considering the energy of stretching the chains, they theoretically estimated the minimum film thickness required for total wetting. Similar extrapolation can be applied to our observation. For polycarbonate patterns with large thickness, reflow happens upon thermal annealing and they finally merge with each other, wetting the substrate totally. When the thickness of the patterns is reduced by oxygen RIE, reflow "ending point" can be observed since the edge of the polymer melts is thin enough and chain stretching is required. As the pattern thickness is on the order of R_g, they can hardly reflow due to the chain entanglement. The radius of gyration of polycarbonate can be estimated by[50] $R_g = 0.038\sqrt{M_w}$, which is 7.3 nm for polycarbonate of molecular weight 36600. The polycarbonate gratings patterned in Fig. 2 are of 30 nm to 40 nm in height, which is 4.1 to 5.5 times of R_g. These data is in accordance with our observation of less reflow with smaller thickness. However currently we are not able to obtain the exact relationship between the final equilibrium state of polymer reflow and polymer thickness. Dynamic simulation work may be needed to address this issue.

Polymer chain stretching needs to be counted only for entangled polymers and the entanglement molecular weight (M_e) of polymers has been reported experimentally and theoretically[45, 46]. We tested step-and-repeat thermal NIL technique towards three polymers available in our lab, which are poly (methyl methacrylate) (PMMA), polystyrene, and polycarbonate of molecular weight 15000, 35000 and 36600, respectively. Based on the reported values of M_e, the molecular weight of the three polymers can be converted as $1.5\times M_e$ for PMMA, $2.8\times M_e$ for polystyrene and $36\times M_e$ for polycarbonate. The temperatures were selected as T_g+50°C for each polymer and only polycarbonate resist is available for thermal step-and-repeat nanoimprint. This can be due to the extremely entangled network of polycarbonate while degree of entanglement may not be enough for PMMA and polystyrene to prevent chains from stretching.

CHAPTER IV

THE APPLICATION OF NANOIMPRINT IN NANOPHOTONICS*

Nanophotonics has emerged as a frontier technology recently, which deals with the behavior of light and its interaction with particles on the nanometer scale. Nanophotonics has drawn huge attention due to its potential applications such as near-field scanning optical microscope, nanophotonic integrated circuits and surface plasmonics. Nanophotonics can be divided into three fields by previous work[51]: nanoscale confinement of matter, nanoscale confinement of radiation and nanoscale photoprocess. In the field of nanoscale confinement of matter, matter is confined to the dimensions of nanoscale to produce unique optical and electrical properties. For example, metallic nanoparticles are able to generate localized surface plasmon, result in large electromagnetic field enhancement near the surface.

---

*Reprinted with permission from "Sensitive surface-enhanced Raman scattering active substrate based on gap surface plasmon polaritons" Jiang, Youwei and Wang, Binhao and Cheng, Xing, Journal of Vacuum Science & Technology B, 32, 012601 (2014). Copyright 2014, American Vacuum Society.

Current SERS and SEIRA techniques are based on rough metallic thin film or solution-processed metallic nanoparticles. One major problem is that the repeatability of enhancement effect is low. Some metallic substrates show huge enhancement, while others have minimal or no enhancement effects. Because of the low repeatability, quantitative analysis such as trace chemical concentrations cannot be done. To expand the usefulness of SERS and SEIRA techniques, highly ordered and high-resolution metallic nanostructures are required for repeatable chemical detection and quantitative analysis.

The applications of nanophotonics thus rely on reliable and dedicated nano-fabrication techniques to produce the metallic nanostructures. Nanoimprint lithography (NIL) could be a strong candidate to provide the desired nanostructure platform for research in nanophotonics. In this work, we present the fabrication of ordered metallic nanostructures by nanoimprint and use various fabricated nanostructures in optical spectroscopy techniques. Based on high resolution nanoimprint lithography, we will investigate the applications of NIL-fabricated nanostructures in surface sensing techniques, surface-enhanced Raman scattering (SERS) and surface-enhanced infrared absorption (SEIRA), which are important branches in nanophotonics. In this chapter, we will present the SERS-active device based on gap surface plasmon polaritons fabricated by nanoimprint lithography. And then the idea of nanoimprinted dipole gold antenna for SEIRA application will be discussed.

4.1 Sensitive SERS substrate based on gap surface plasmon polaritons

4.1.1 Raman spectropy and surface-enhanced Raman scattering

When a beam of light is interacting with a material, part of it will be reflected, part will be transmitted and the remaining will be scattered. Most photons in the scattered part have exactly the same frequency as the incident photons, which is referred as elastic scattering or Rayleigh scattering. At the same time, there is only a small fraction of photons with different frequency as the incident photons after scattering. And this is referred as inelastic scattering or Raman scattering. For the scattering in which the energy of the scattered photons is shifted down, it is named Stokes scattering while anti-Stokes scattering for the other case. The energy shift of Raman scattering delivers information of molecular vibration and Raman spectropy is the very technique to collect Raman scattering signal and observe vibrational, rotational and other low-frequency modes. In practical, a laser beam, usually from visible range, is focused on the material and the scatted light is then collected through a lens. The scattered light with the same frequency of the incident light, due to Rayleigh scattering, will be filtered and the rest, due to Raman scattering, will be collected. The field intensity of the scattered light corresponding to the wavelength shift of the scattered light to the incident light is then analyzed and plotted as the Raman spectrum.

Note that Raman scattering is typically very weak, it requires the intensity of the scattered light to be large enough for high quality spectrum. In other words, high sensitivity is required in detection applications when the concentration of the specimen

is low. Surface-enhanced Raman spectropy is an advanced Raman spectropy technique that can enhance the Raman scattering signal by the molecule on the rough metal surface. The mechanism of SERS is still in debate currently and there are two main streams of theories, electromagnetic mechanism and chemical theory, in which electromagnetic mechanism has been widely investigated and discussed due to its simplicity and accordance with most observations. As the incident light interacts with a small metallic particle with the feature size smaller than the wavelength of the incident light, the metallic particle will excite and sustain surface plasmon, which is the collective oscillation of electrons corresponding to the metal nuclei. When the frequency of surface plasmon is equal to the frequency of the incident light, a state of resonance, referred as localized surface plasmon resonance, is established and the field intensity around the metallic particle is maximized[52].

4.1.2 Surface-enhanced Raman scattering and gap surface plasmon polaritons

Surface-enhanced Raman scattering (SERS)[53, 54] has important applications in chemical and biological sensing techniques. It is generally understood that two mechanisms - electromagnetic (EM) enhancement[55] and chemical enhancement[56, 57] - contribute to the SERS effect, and the EM enhancement is believed to be dominant. It has been well studied that the EM enhancement results from the excitation of localized surface plasmons (LSPs) at metal nanoparticles, which provides an increase of electromagnetic field on metal surfaces. Substrates with irregular nanoscale features have been widely used as SERS-active substrates, including roughened metal substrate[58] or other features

covered by evaporated metal film[59]. Although single molecule detection has been reported[53] based on pairs of nanoparticles which are extremely close to each other, these techniques rely on the randomly distributed "hot spot"[60, 61] and suffer from poor uniformity and reproducibility. Moreover, large scale area-average performance is not available for non-uniform SERS substrate, which is not desirable for practical application. SERS substrate with regular nanostructure array[62-66] has drawn more attention to overcome the drawbacks of the above techniques. However theoretical calculation of a silver dimer system indicated that a gap size on the order of 1 nm to 2 nm dimer spacing is needed to achieve large enhancement,[67] which is extremely difficult to fabricate. Gap surface plasmon polaritons (GSPPs)[68-70] are excited at the dielectric gap region sandwiched by two metal surfaces. The previous work in our group[71] has numerically demonstrated that GSPPs can result in strong local field enhancement at the metal/dielectric interfaces. Although a thin layer of dielectric is preferred for large enhancement,[72] it is generally easy to control the thickness of a thin film with high precision by thin-film deposition techniques.

The issue of gap surface plamson polaritons (GSPP) can be treated as s multilayer system consisting of alternating metal and insulator layers, where each surface sustains surface plasmon polaritons (SPP). While two interfaces are close enough, that is smaller than the decay distance (normal to the propagation direction) of a single SPP, SPPs begin to couple and GSPP mode needs to be considered. Metal/insulator/metal (MIM) and insulator/metal/insulator (IMI) are two typical geometries of the multilayer system

and we focus only on metal/insulator/metal structure due to its application in surface-enhanced Raman scattering. A simple model of metal/insulator/metal structure is given by Figure 26. Theoretical calculation incorporating Maxwell equation demonstrates that large wave vector can be achieved at a single insulator/metal surface even for excitation well below the resonance frequency, given a very thin gap (the insulator layer). Due to the easy fabrication of a uniform thin metal or insulator layer, MIM and IMI structures have found promising applications in surface sensing technique and wave guiding. Chu and Crozier have experimentally investigated the interaction of LSP and PSP in a gold nanostructure/ SiO_2/ gold layer structure[73]. The previous work[71] in our group reported an enhancement factor up to 10^{11} based on silver nanostructure/ SiO2/ silver layer structure by FDTD simulation. For applications of wave guiding, GSPP-based waveguide[69, 74, 75] and resonator[72, 76, 77] have been widely investigated. In this chapter, we experimentally and numerically investigated the SERS effect with silver structures on SiO_2 spacer deposited on a bottom silver layer. Three types of structures were fabricated to demonstrate the large enhancement effect resulted from the GSPPs.

4.1.3 Experimental details

GSPPs are generally supported by metal-insulator-metal (MIM) or insulator-metal-insulator (IMI) multilayer system.[76] Figure 25 illustrates our fabricated structures. The type 1 structure is similar to a surface-patterned silver layer, which is typical in SERS-active substrates. In type 2 and 3 substrates, GSPPs can be excited by the MIM structures where a SiO_2 dielectric layer is sandwiched by a silver pattern on the top and a

thick silver layer at the bottom. In type 2 substrate, the silver pattern is fabricated on top of a uniform SiO_2 spacer layer, while in type 3 both the SiO_2 spacer and the top silver layer are patterned on the bottom silver layer. The top silver surface patterns are 600 nm by 600 nm squares with 700 nm pitch and the thickness of the top silver layer, the SiO_2 spacer and the bottom silver layer are 40 nm, 20 nm, and 200 nm, respectively.

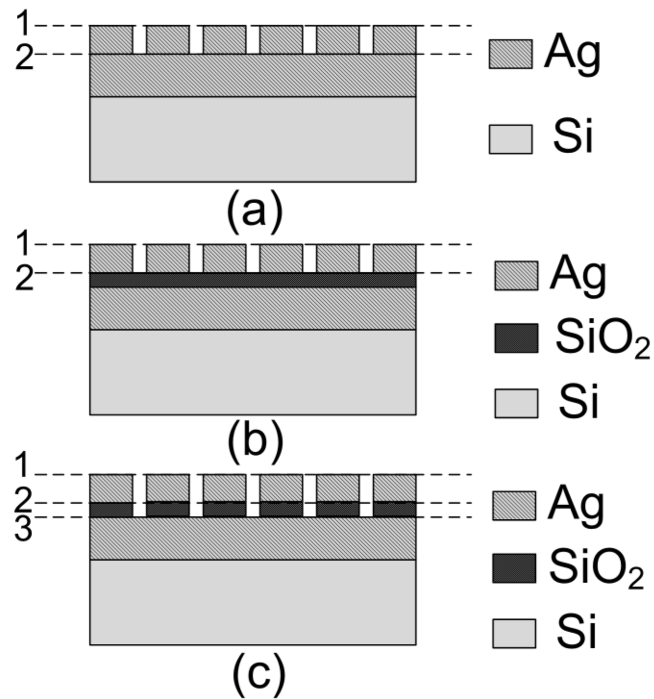

Figure 25. Schematics of three different SERS-active substrates: (a) type 1, a conventional SERS-active substrate with silver grids on the bottom silver layer; (b) type 2, a uniform SiO_2 spacer sandwiched between the top silver grids and the bottom silver layer; and (c) type3, both top silver grids and the SiO_2 spacer are patterned on the bottom silver layer. The interfaces are labelled as 1, 2 and 3 for easy reference in the discussion section.

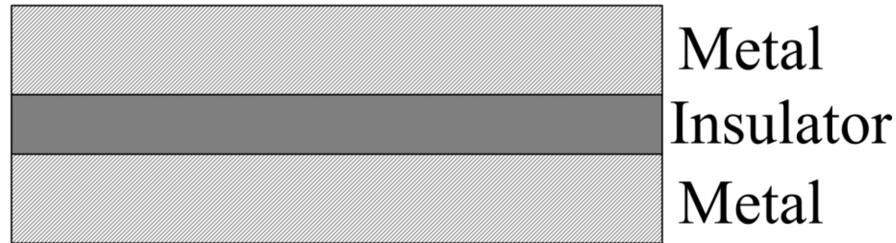

Figure 26. The schematic of metal/insulator/metal structure.

The fabrication of the proposed structures was accomplished by nanoimprint lithography, reactive-ion etching, electron-beam evaporation and metal lift-off process, as shown in Figure 27. The nanoimprint mold used in the experiments was home-made SiO_2 mold with 600 nm square grids with 700 nm pitch. The depth of the features was 200 nm. For all SERS substrates, the 200 nm bottom silver layer was deposited by electron-beam evaporation (Kurt J. Lesker PVD 75 thin film deposition system) onto Si wafer. In type 1 substrate, PMMA (from Sigma-Aldrich, M_w=15k) resist was spin-coated on the bottom silver layer and patterned by nanoimprint lithography (Figure 27 (b1)), followed by oxygen reactive-ion etch to remove the residue layer (Figure 27(c1)). After that, the top silver structures were fabricated by electron-beam evaporation of 40 nm silver (Figure 27 (d1)) and lift-off in acetone (Figure 27 (e1)). In type 2 substrate, a SiO_2 spacer layer was evaporated onto the bottom silver layer before the top silver structures were defined (Figure 27 (b2-e2)). In type 3 substrate, the SiO_2 spacer layer and the top silver layer

were sequentially evaporated after the PMMA structures were fabricated (Figure 27(d3)), yielding the patterned stacking layers of SiO_2 and silver (Figure 27 (e3)).

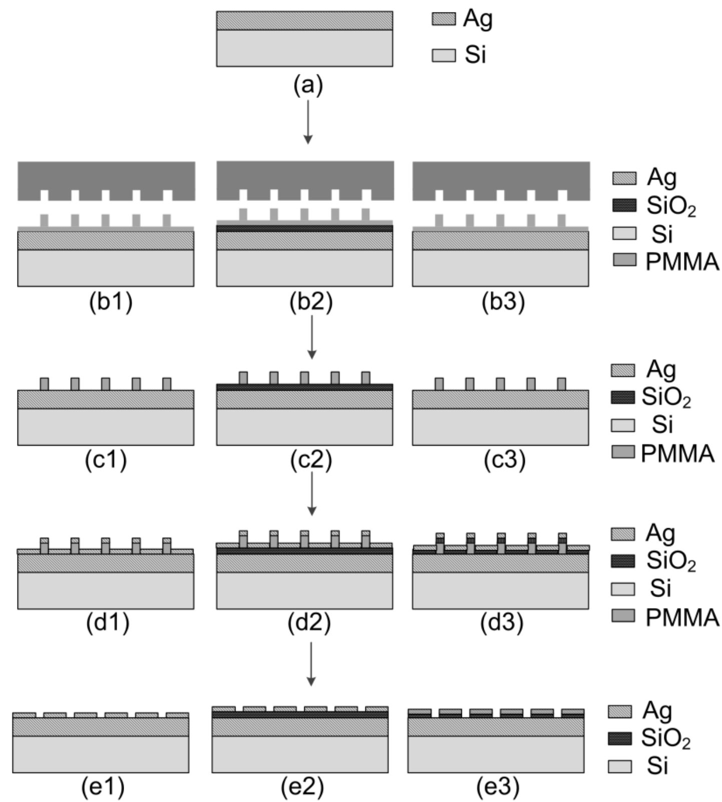

Figure 27. Schematics of the fabrication flow for type 1,2 and 3 SERS-active substrates: (a) 200 nm bottom silver layer evaporation on Si wafer; (b2) 20 nm SiO_2 spacer evaporation on bottom silver layer and (b) PMMA pattern definition by nanoimprint lithography; (c) oxygen reactive ion etching to remove the residual layer; (d1),(d2) 40 nm top silver layer evaporation and (d3) sequential evaporation of 20nm SiO_2 spacer and 40 nm top silver layer; (e) lift-off process in acetone with ultrasound agitation.

4.1.4 Raman spectropy on SERS substrates

In order to evaluate the SERS enhancement effect, all SERS substrates were incubated in 1mM thiophenol (from Sigma-Aldrich) solution in methanol for 30 min to allow the formation of self-assembled monolayer on silver[78]. All samples were rinsed in methanol to remove non-absorbed thiophenol molecules on the surface and then dried by nitrogen gas and hot plate. For calculation of the area-averaged enhancement factor, a reference sample without SERS effect was prepared by applying a certain amount of thiophenol liquid on 30 nm aluminum, which was deposited on a glass slide by electron beam evaporation. The thiophenol liquid was weighed by Mettler Toledo ML204 balance with 0.1 mg precision. Then the reference sample was immediately transferred for Raman spectra. Raman spectroscopy was performed by Horiba Jobin-Yvon LabRam IR system using fixed parameters for all samples. The experiments were conducted with 633 nm laser wavelength.

The SEM top view of the fabricated type 2 substrate is shown in Figure 28. The type 3 substrate looks the same in the SEM top view. Figure 29 shows the Raman spectra for all three types of substrates and the reference sample (scaled down by 10^{-2}). The 1072 cm^{-1} peak of thiophenol is investigated and its intensity is labeled in each spectrum. Given that the Raman spectra was taken using fixed conditions for all samples, the area-averaged SERS enhancement factor (EF) is given by

$$EF = \frac{I_{SERS} / N_{SERS}}{I_{ref} / N_{ref}}$$

where N_{SERS} and N_{ref} are the number of molecules probed on the SERS substrates and the reference sample; I_{SERS} and I_{ref} are the peak intensities of the Raman spectra from SERS substrates and the reference sample. For the reference sample, 20.7 mg thiophenol liquid was applied on the aluminum surface and spread as a round shape with a diameter of 0.47 cm. The diameter of the 633nm laser beam is 10 μm. Assuming a uniform molecule distribution within the thiophenol droplet of the reference sample, N_{ref} can be estimated as 1.2×10^{16} molecules. For SERS substrates, by assuming thiophenol packing density of 6.8×10^{14} molecules/ cm^2 [63] and calculating the area of silver surface which is accessible to the thiophenol molecules, N_{SERS} is approximately calculated as $N_{SERS,1}=N_{SERS,3}=6.4\times10^8$ molecules and $N_{SERS,2}=4.9\times10^8$. By substituting the peak intensity for SERS substrates and the reference sample, the area-averaged EF is calculated as $EF_{SERS,1}=6.2\times10^5$, $EF_{SERS,2}=5.2\times10^6$, $EF_{SERS,3}=1.1\times10^7$. Meanwhile we need to point out that the calculation above is a rough estimation. Deviation can be introduced by factors such as the non-uniform optical field distribution in the laser focal spot, assumption of complete and uniform thiophenol monomer adsorbed on silver surface and pattern dimension variation introduced by the fabrication processes.

Compared with type 1 substrate, which is the conventional SERS-active substrate consisting of silver structures, larger area-averaged EFs are obtained in type 2 and 3 substrates, in which a 20 nm SiO_2 spacer is sandwiched between the silver structures and the bottom silver layer. Figure 30 shows the plots of field intensity distribution along the edge of the interfaces from different substrates (see Figure 25 for interface labeling).

It is observed that for the GSPPs-based structures, more optical energy resides at the interface of the top silver layer and the SiO_2 spacer. Moreover, the maximum field intensities of type 2 and type 3 are much larger than that of conventional SERS-active substrate, agreeing with the calculation of the area-averaged enhancement factors for all samples.

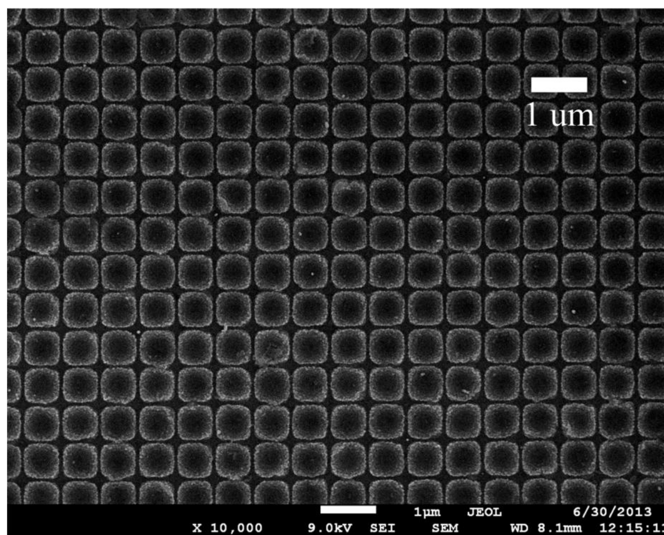

Figure 28. The SEM top view of fabricated type 2 SERS-active substrate by nanoimprint. The scale bar is 1 um.

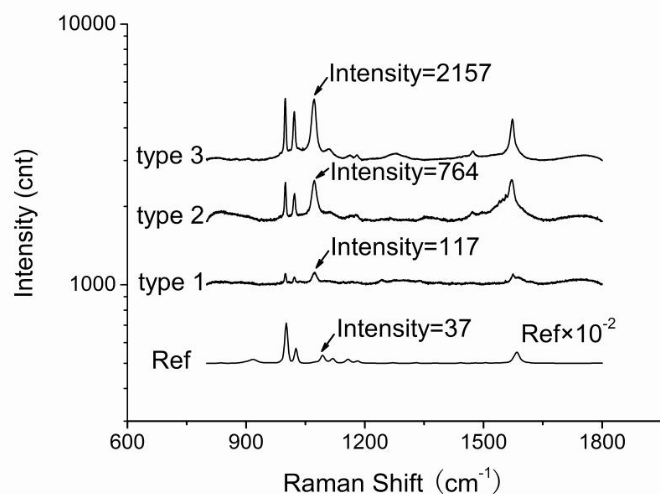

Figure 29. Raman spectra of thiophenol from type 1, type 2, type 3 SERS-active substrates and the reference sample (scaled down by 10^{-2}). The intensity of 1072 cm^{-1} peak is labeled. All spectra were collected under the same conditions.

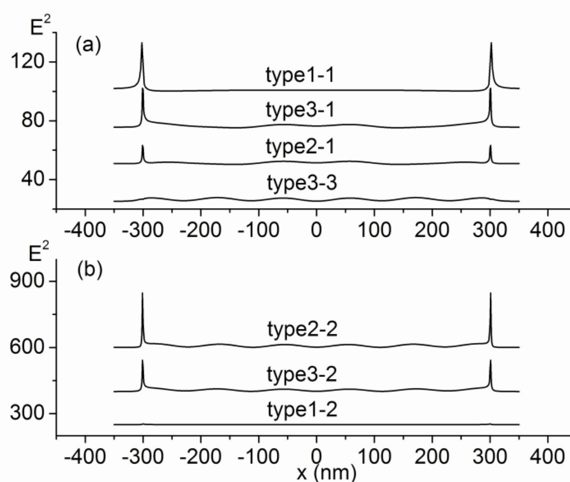

Figure 30. Plots of field intensity distribution along the interfaces of different substrates (See Fig.25 for interface labeling). The dimension of all top patterns is 600 nm and the wavelength of the incident light is 633 nm. All plots are taken from the edge of the interface. The values of the peak intensities are 33.0 (type 1-1), 27.1 (type 3-1), 13.3 (type 2-1), 2.7 (type 3-3) in (a) and 246.7 (type 2-2), 142.5 (type 3-2), 3.6 (type 1-2) in (b).

The extra Raman signal intensity enhancement in type 2 substrate can be explained by the existence of the GSPPs. In GSPPs-based substrates, there exist two individual SPPs at the interface between the SiO_2 spacer and the top silver grid structure, and the interface between the SiO_2 spacer and the bottom silver layer. The SPPs from both interfaces interact within the thin SiO_2 spacer layer and a large field enhancement can be obtained due to the coupling effect. It has been demonstrated that a large propagation constant can be achieved for excitation well deviating from the resonant frequency, given that the SiO_2 spacer is thin enough.[79] Moreover, the interaction between the LSPs in the top silver structure and the propagating SPPs at the surface of the bottom silver layer also plays a role in the field enhancement.[73] The type 3 substrate exhibits even larger enhancement than type 2 despite of smaller field intensity in Figure 30(b). This can result from several factors. First, although the maximum field intensity of type 3 is smaller than that of type 2 at the silver/SiO_2 interface, much larger field intensity is observed at the top region of silver structures in type 3 (Figure 30(a)). Given that the maximum intensity is located within the very corner region of the silver/SiO_2 interface (56% percent intensity attenuation is observed 1 nm away from the peak position), the electric field in the top region of the silver structures can also contribute to the area-averaged enhancement. Second, compared with type 2 substrate, more molecules are accessible to the bottom silver layer in type 3 with the existence of the GSPPs. However, in order to precisely evaluate the area-averaged enhancement factor from FDTD calculation, every single site occupied by a molecule and its corresponding field intensity needs to be considered and synthesized as a whole. We are not able to achieve

this in this work and more effort is required for quantitative investigation of area-averaged enhancement factor.

The GSPPs-based SERS-active substrates exhibit larger enhancement compared with conventional LSP-based substrates with the same dimension based on our experiments. For GSPPs and LSP substrates with similar performance, the LSP substrates are dominated by the fabrication limitation. In order to achieve $E^4=10^{10}$, 2 nm separation is required for the silver dimer system[67], which demands at least 2 nm fabrication precision. At the same time, similar performance can be achieved by GSPPs-based substrates with a lateral structure on the order of 100 nm and a vertical SiO_2 spacer thickness of 20 nm[71], which can be easily fabricated by electron-beam lithography and thin-film deposition.

4.1.5 Device optimization and discussion

Two important factors should be taken into consideration for the optimization of the GSPP substrates. First, the thickness of the SiO_2 spacer needs to be well controlled to support the GSPPs. On one hand, very thick SiO_2 spacer is not desired since the coupling of the two SPPs dampens significantly when the spacer thickness increases. It has been demonstrated that for a system with a dielectric gap sandwiched by a silver nanostripe and a silver plate, smaller field intensity is observed for 80 nm gap, compared with 10 nm and 30 nm gap.[72] FDTD calculations based on type 2 substrate illustrate the coupling effect of the SPPs with varying SiO_2 thickness. The field distributions of the type 2 substrates with 20 nm, 50 nm and 80 nm SiO_2 spacer are shown in Figure 31. It is

observed that the strong coupling yields more intense electromagnetic field in 20 nm spacer than in both 50 nm and 80 nm spacers, where only weak couplings are observed.

On the other hand, although larger propagation constant is expected for smaller gap, it is indicated that a significant amount of the field energy of the GSPPs resides in the metal, provided that the gap is sufficiently small[79]. Since the field intensity at the metal/dielectric interface where molecules interact with the light is of importance in the GSPP structures, very thin SiO_2 spacer yields lower field intensity, as shown in our previous numerical investigation of the relationship between the SiO_2 spacer thickness and the SERS enhancement factor.[71] The second important factor in the GSPP substrate design is the shape and dimension of the structures in the top silver layer. The relationship between the excitation wavelength and the resonance size of the nanostructure has been widely studied.[63, 77] Although the structures in this work are limited to 600 nm square patterns with 700 nm pitch due to the availability of the mold used in nanoimprint, further improvement is assured by modifying the shape and size of the structures, as discussed in our previous work.[71] These nanostructures can be fabricated by e-beam lithography[73, 80] and nanoimprint lithography[65, 66]. Furthermore, Chu and Crozier [22] indicated that the coupling between the LSPs, which are supported by metal particles, and the propagating surface plasmons (PSPs), which are supported by the continuous metal film, could lead to strong field enhancement when the resonance frequencies of the LSPs and PSPs were tuned approximately equal. The resonance

frequency of the LSPs can be adjusted by changing the particle size as well as the periodicity of the metal particle array.

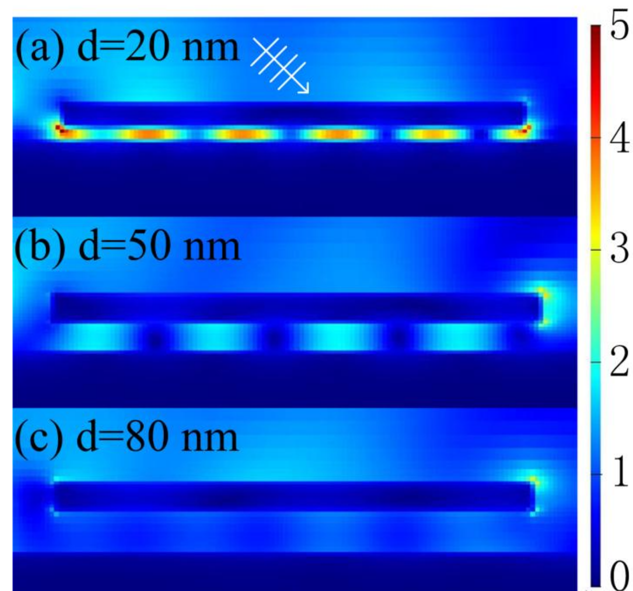

Figure 31. FDTD calculation of intensity distribution of type 2 substrate with (a) 20 nm SiO_2 spacer; (b) 50 nm SiO_2 spacer and (c) 80 nm SiO_2 spacer. The arrow represents the propagating direction of the incident light.

CHAPTER V

SUMMARY

Nanoimprint lithography (NIL) has been considered as one of the most promising techniques for next generation lithography techniques due to its high resolution and low cost. The potential of NIL relies on high quality mold fabrication. Conventionally electron beam lithography is used for mold fabrication. However this method suffers from low throughput and high cost, especially for high density patterning. In this work, we have developed two unique techniques for high resolution NIL mold fabrication, which are polyelectrolyte electrostatic self-assembly and polymer controlled reflow. These methods are featured with high resolution and low cost.

Based on the observation of polymer reflow, we have figured out that polycarbonate thin film exhibits exceptional thermal stability upon high temperature annealing due to polymer chain entanglement. Two potential applications have been developed, which are high resolution patterning and step-and-repeat thermal NIL. Polymer gratings with resolution up to 35 nm were fabricated and pattern transfer is also available for mold fabrication. For step-and-repeat thermal NIL application, the throughput was improved by six times compared with conventional thermal NIL and the capability of large-scale application was also demonstrated.

The capability of high density and high resolution patterning of NIL rises up possibilities for surface sensing techniques. The applications of ordered metallic nanoparticles on surface-enhanced Raman scattering (SERS) have been widely investigated. In order to achieve high enhancement, extremely high resolution nanostructures are desirable, which may be even beyond the lithography limitation. SERS devices based on gap surface plasmon polaritons (GSPPs) could provide considerable enhancement effect without extremely high resolution lithography requirements. In this work, we fabricated SERS devices based on GSPPs and compared their performance with conventional SERS devices. A performance improvement up to 17 times can be achieved for GSPPs-based devices under the same structure dimensions. Device optimization has also been discussed using FDTD calculation.

REFERENCES

[1]S. Y. Chou, P. R. Krauss and P. J. Renstrom, Journal of Vacuum Science & Technology B: Microelectronics and Nanometer Structures **14**, 4129-4133 (1996).

[2]L. J. Guo, Advanced Materials **19**, 495-513 (2007).

[3]S. W. Pang, T. Tamamura, M. Nakao, A. Ozawa and H. Masuda, Journal of Vacuum Science & Technology B **16**, 1145-1149 (1998).

[4]J. Taniguchi, Y. Tokano, I. Miyamoto, M. Komuro and H. Hiroshima, Nanotechnology **13**, 592 (2002).

[5]B. D. Gates, Q. Xu, M. Stewart, D. Ryan, C. G. Willson and G. M. Whitesides, Chemical Reviews **105**, 1171-1196 (2005).

[6]G. Decher, Science **277**, 1232-1237 (1997).

[7]C. Figura, P. J. Neyman, D. Marciu, C. Brands, M. A. Murray, S. Hair, R. M. Davis, M. B. Miller and J. R. Heflin, presented at the Symposium on Integrated Optoelectronics, 2000 (unpublished).

[8]C. Srinivasan, J. Hohman, M. Anderson, P. Weiss and M. Horn, Journal of Vacuum Science & Technology B: Microelectronics and Nanometer Structures **25**, 1985-1988 (2007).

[9]A. B. Artyukhin, O. Bakajin, P. Stroeve and A. Noy, Langmuir **20**, 1442-1448 (2004).

[10]S. D. Evans, A. Ulman, K. E. Goppert-Berarducci and L. J. Gerenser, Journal of the American Chemical Society **113**, 5866-5868 (1991).

[11]R. L. Jones, T. Hu, C. L. Soles, E. K. Lin, R. M. Reano, S. W. Pang and D. M. Casa, Nano letters **6**, 1723-1728 (2006).

[12]Y. Ding, H. W. Ro, J. F. Douglas, R. L. Jones, D. R. Hine, A. Karim and C. L. Soles, Advanced Materials **19**, 1377-1382 (2007).

[13]T. Leveder, E. Rognin, S. Landis and L. Davoust, Microelectronic Engineering **88**, 1867-1870 (2011).

[14]V. J. Novotny, The Journal of Chemical Physics **92**, 3189-3196 (1990).

[15]P. Silberzan and L. Leger, Macromolecules **25**, 1267-1271 (1992).

[16]B. Frank, A. P. Gast, T. P. Russell, H. R. Brown and C. Hawker, Macromolecules **29**, 6531-6534 (1996).

[17]W. Zhao, M. H. Rafailovich, J. Sokolov, L. J. Fetters, R. Plano, M. K. Sanyal, S. K. Sinha and B. B. Sauer, Physical Review Letters **70**, 1453-1456 (1993).

[18]P. Lomellini, Die Makromolekulare Chemie **193**, 69-79 (1992).

[19]Y. Ding, H. Wook Ro, T. A. Germer, J. F. Douglas, B. C. Okerberg, A. Karim and C. L. Soles, ACS Nano **1**, 84-92 (2007).

[20]H. Yoon, H. S. Cho, K. Y. Suh and K. Char, Nanotechnology **21** (2010).

[21]M. Colburn, S. C. Johnson, M. D. Stewart, S. Damle, T. C. Bailey, B. Choi, M. Wedlake, T. B. Michaelson, S. V. Sreenivasan, J. G. Ekerdt and C. G. Willson, 1999 (unpublished).

[22]E. A. Costner, M. W. Lin, W.-L. Jen and C. G. Willson, Annual Review of Materials Research **39**, 155-180 (2009).

[23]I. McMackin, J. Choi, P. Schumaker, V. Nguyen, F. Xu, E. Thompson, D. Babbs, S. Sreenivasan, M. Watts and N. Schumaker, presented at the Proc. of SPIE Vol, 2004 (unpublished).

[24]D. J. Resnick, S. Sreenivasan and C. G. Willson, Materials Today **8**, 34-42 (2005).

[25]T. Haatainen, T. Mäkelä, J. Ahopelto and Y. Kawaguchi, Microelectronic engineering **86**, 2293-2296 (2009).

[26]T. Haatainen, T. Mäkelä, A. Schleunitz, G. Grenci and M. Tormen, Microelectronic Engineering **98**, 180-183 (2012).

[27]H. Yoon, H. Cho, K. Suh and K. Char, Nanotechnology **21**, 105302 (2010).

[28]D. Y. Khang, H. Yoon and H. H. Lee, Advanced Materials **13**, 749-752 (2001).

[29]J. Xu, L. Locascio, M. Gaitan and C. S. Lee, Analytical chemistry **72**, 1930-1933 (2000).

[30]S. Harrer, J. K. Yang, G. A. Salvatore, K. K. Berggren, F. Ilievski and C. A. Ross, Nanotechnology, IEEE Transactions on **6**, 639-644 (2007).

[31]C. Chu and G. N. Parsons, Journal of Vacuum Science & Technology B **24**, 818-822 (2006).

[32]L. Tan, Y. Kong, S. Pang and A. Yee, Journal of Vacuum Science & Technology B: Microelectronics and Nanometer Structures **22**, 2486-2492 (2004).

[33]R. Bruinsma, Macromolecules **23**, 276-280 (1990).

[34]J. Emsley, Chemical Society Reviews **9**, 91-124 (1980).

[35]P.-G. De Gennes, Reviews of modern physics **57**, 827 (1985).

[36]X. Zheng, B. Sauer, J. Van Alsten, S. Schwarz, M. Rafailovich, J. Sokolov and M. Rubinstein, Physical review letters **74**, 407 (1995).

[37]Q. Lan, J. Yu, J. Zhang and J. He, Macromolecules **44**, 5743-5749 (2011).

[38]X. Liang, T. Chen, Y.-S. Jung, Y. Miyamoto, G. Han, S. Cabrini, B. Ma and D. L. Olynick, ACS nano **4**, 2627-2634 (2010).

[39]Z. Hu, G. Baralia, V. Bayot, J.-F. Gohy and A. M. Jonas, Nano letters **5**, 1738-1743 (2005).

[40]R. Farmer, Virginia Polytechnic Institute and State University, 2001.

[41]F. Gallez, R. Legras and J. Mercier, Journal of Polymer Science: Polymer Physics Edition **14**, 1367-1377 (1976).

[42]P. E. Rouse Jr, The Journal of Chemical Physics **21**, 1272 (1953).

[43]K. Kremer and G. S. Grest, The Journal of Chemical Physics **92**, 5057-5086 (1990).

[44]R. H. Colby, L. J. Fetters and W. W. Graessley, Macromolecules **20**, 2226-2237 (1987).

[45]L. Fetters, D. Lohse, D. Richter, T. Witten and A. Zirkel, Macromolecules **27**, 4639-4647 (1994).

[46]S. Wu, Polymer Engineering & Science **32**, 823-830 (1992).

[47]H. Watanabe, Progress in Polymer Science **24**, 1253-1403 (1999).

[48]P.-G. De Gennes, F. Brochard-Wyart and D. Quéré, *Capillarity and wetting phenomena: drops, bubbles, pearls, waves*. (Springer, 2004).

[49]W. Zhao, M. Rafailovich, J. Sokolov, L. Fetters, R. Plano, M. Sanyal, S. Sinha and B. Sauer, Physical review letters **70**, 1453 (1993).

[50]W. Gawrisch, M. Brereton and E. Fischer, Polymer Bulletin **4**, 687-691 (1981).

[51]Y. Shen, C. S. Friend, Y. Jiang, D. Jakubczyk, J. Swiatkiewicz and P. N. Prasad, The Journal of Physical Chemistry B **104**, 7577-7587 (2000).

[52]K. L. Kelly, E. Coronado, L. L. Zhao and G. C. Schatz, The Journal of Physical Chemistry B **107**, 668-677 (2003).

[53]K. Kneipp, Y. Wang, H. Kneipp, L. T. Perelman, I. Itzkan, R. R. Dasari and M. S. Feld, Phys Rev Lett **78**, 1667-1670 (1997).

[54]M. Moskovits, Rev Mod Phys **57**, 783-826 (1985).

[55]H. Xu, J. Aizpurua, M. Käll and P. Apell, Physical Review E - Statistical Physics, Plasmas, Fluids, and Related Interdisciplinary Topics **62**, 4318-4324 (2000).

[56]W. E. Doering and S. Nie, J Phys Chem B **106**, 311-317 (2002).

[57]A. T. Zayak, Y. S. Hu, H. Choo, J. Bokor, S. Cabrini, P. J. Schuck and J. B. Neaton, Phys Rev Lett **106**, 083003 (2011).

[58]Z. Q. Tian, B. Ren and D. Y. Wu, J Phys Chem B **106**, 9463-9483 (2002).

[59]J. G. Fan and Y. P. Zhao, Langmuir **24**, 14172-14175 (2008).

[60]W. Li, P. H. C. Camargo, X. Lu and Y. Xia, Nano Letters **9**, 485-490 (2009).

[61]S. J. Lee, A. R. Morrill and M. Moskovits, J Am Chem Soc **128**, 2200-2201 (2006).

[62]H. Wang, C. S. Levin and N. J. Halas, J Am Chem Soc **127**, 14992-14993 (2005).

[63]A. D. McFarland, M. A. Young, J. A. Dieringer and R. P. Van Duyne, The Journal of Physical Chemistry B **109**, 11279-11285 (2005).

[64]R. Alvarez-Puebla, B. Cui, J. P. Bravo-Vasquez, T. Veres and H. Fenniri, Journal of Physical Chemistry C **111**, 6720-6723 (2007).

[65]W. D. Li, F. Ding, J. Hu and S. Y. Chou, Opt Express **19**, 3925-3936 (2011).

[66]B. Cui, L. Clime, K. Li and T. Veres, Nanotechnology **19** (2008).

[67]E. Hao and G. C. Schatz, The Journal of chemical physics **120**, 357 (2004).

[68]P. Neutens, P. Van Dorpe, I. De Vlaminck, L. Lagae and G. Borghs, Nature Photonics **3**, 283-286 (2009).

[69]B. Wang and G. P. Wang, Optics letters **29**, 1992-1994 (2004).

[70]S. I. Bozhevolnyi, J. Erland, K. Leosson, P. M. W. Skovgaard and J. M. Hvan, Phys Rev Lett **86**, 3008-3011 (2001).

[71]H. C. Kim and X. Cheng, Optics Express **17**, 17234-17241 (2009).

[72]J. Jung, T. Søndergaard and S. I. Bozhevolnyi, Physical Review B - Condensed Matter and Materials Physics **79** (2009).

[73]Y. Chu and K. B. Crozier, Optics letters **34**, 244-246 (2009).

[74]S. A. Maier, Optics communications **258**, 295-299 (2006).

[75]S. I. Bozhevolnyi, J. Erland, K. Leosson, P. M. Skovgaard and J. M. Hvam, Physical Review Letters **86**, 3008 (2001).

[76]S. I. Bozhevolnyi and T. Søndergaard, Opt Express **15**, 10869-10877 (2007).

[77]G. Della Valle, T. Sondergaard and S. I. Bozhevolnyi, Opt Express **16**, 6867-6876 (2008).

[78]L.-J. Wan, M. Terashima, H. Noda and M. Osawa, The Journal of Physical Chemistry B **104**, 3563-3569 (2000).

[79]S. A. Maier, *Plasmonics: Fundamentals and Applications*. (2007).

[80]C. L. Haynes, A. D. McFarland, L. Zhao, R. P. Van Duyne, G. C. Schatz, L. Gunnarsson, J. Prikulis, B. Kasemo and M. Käll, The Journal of Physical Chemistry B **107**, 7337-7342 (2003).